The Homogenized Energy Model (HEM) for Characterizing Polarization and Strains in Hysteretic Ferroelectric Materials: Implementation Algorithms and Data-Driven Parameter Estimation Techniques

Zhengzheng Hu and Ralph C. Smith
Department of Mathematics
Center for Research in Scientific Computation
North Carolina State University
Raleigh, NC 27695

Jon Ernstberger
Department of Mathematics
LaGrange College
LaGrange, GA 30240

Abstract

Ferroelectric materials, such as PZT, PLZT, PMN and $BaTiO_3$, provide unique actuator and sensor capabilities for applications including nanopositioning, high speed valves and fuel injectors, camera focusing and shutter mechanisms, ultrasonic devices for biomedical imaging and treatment, and energy harvesting devices. However, to achieve the full potential of the materials, it is necessary to develop and employ models that quantify the creep, rate-dependent hysteresis, and constitutive nonlinearities that are intrinsic to the materials due to their domain structure. The success of models requires that they be highly efficient to implement since real-time applications can require kHz to MHz rates. The calibration of models for specific materials, devices, and applications, requires efficient and robust parameter estimation algorithms. Finally, control designs can be facilitated by models that admit efficient and robust approximate inversion. The homogenized energy model (HEM) is a multiscale, micromechanical framework that quantifies a range of hysteretic phenomena intrinsic to ferroelectric, ferromagnetic and ferroelastic materials. In this paper, we present highly efficient implementation and parameter estimation algorithms for the ferroelectric model. This includes techniques to construct analytic Jacobians and data-driven algorithms to determine initial parameter estimates to facilitate subsequent optimization. The efficiency of these algorithms facilitates material and device characterization and provides the basis for constructing efficient and robust inverse algorithms for model-based control design. The model implementation, calibration, and validation are illustrated using rate-dependent PZT data and single crystal $BaTiO_3$ data.

Report Documentation Page

1. REPORT DATE **JAN 2012**	2. REPORT TYPE	3. DATES COVERED **00-00-2012 to 00-00-2012**

4. TITLE AND SUBTITLE **The Homogenized Energy Model (HEM) for Characterizing Polarization and Strains in Hysteretic Ferroelectric Materials: Implementation Algorithms and Data-Driven Parameter Estimation Techniques**	5a. CONTRACT NUMBER
	5b. GRANT NUMBER
	5c. PROGRAM ELEMENT NUMBER

6. AUTHOR(S)	5d. PROJECT NUMBER
	5e. TASK NUMBER
	5f. WORK UNIT NUMBER

7. PERFORMING ORGANIZATION NAME(S) AND ADDRESS(ES) **North Carolina State University,Center for Research in Scientific Computation,Department of Mathematics,Raleigh,NC,27695-8212**	8. PERFORMING ORGANIZATION REPORT NUMBER **CRSC-TR12-02**

9. SPONSORING/MONITORING AGENCY NAME(S) AND ADDRESS(ES)	10. SPONSOR/MONITOR'S ACRONYM(S)
	11. SPONSOR/MONITOR'S REPORT NUMBER(S)

12. DISTRIBUTION/AVAILABILITY STATEMENT
Approved for public release; distribution unlimited

13. SUPPLEMENTARY NOTES

14. ABSTRACT

Ferroelectric materials, such as PZT, PLZT, PMN and BaTiO3, provide unique actuator and sensor capabilities for applications including nanopositioning, high speed valves and fuel injectors camera focusing and shutter mechanisms, ultrasonic devices for biomedical imaging and treatment and energy harvesting devices. However, to achieve the full potential of the materials, it is necessary to develop and employ models that quantify the creep, rate-dependent hysteresis, and constitutive nonlinearities that are intrinsic to the materials due to their domain structure. The success of models requires that they be highly efficient to implement since real-time applications can require kHz to MHz rates. The calibration of models for specific materials, devices, and applications, requires efficient and robust parameter estimation algorithms. Finally, control designs can be facilitated by models that admit efficient and robust approximate inversion. The homogenized energy model (HEM) is a multiscale, micromechanical framework that quantifies a range of hysteretic phenomena intrinsic to ferroelectric, ferromagnetic and ferroelastic materials. In this paper, we present highly efficient implementation and parameter estimation algorithms for the ferroelectric model. This includes techniques to construct analytic Jacobians and data-driven algorithms to determine initial parameter estimates to facilitate subsequent optimization. The efficiency of these algorithms facilitates material and device characterization and provides the basis for constructing efficient and robust inverse algorithms for model-based control design. The model implementation, calibration and validation are illustrated using rate-dependent PZT data and single crystal BaTiO3 data.

15. SUBJECT TERMS

16. SECURITY CLASSIFICATION OF:			17. LIMITATION OF ABSTRACT	18. NUMBER OF PAGES	19a. NAME OF RESPONSIBLE PERSON
a. REPORT **unclassified**	b. ABSTRACT **unclassified**	c. THIS PAGE **unclassified**	**Same as Report (SAR)**	**35**	

Nomenclature

d	Piezoelectric constant (m/V = C/N)
h	Piezoelectric constant (V/m = N/C)
E	Electric field (V/m)
g	Gibbs energy for dipoles (CV)
G_α	Gibbs energy density of α-variant (CV/m^3)
G_α^e	Electric Gibbs energy density of α-variant (CV/m^3)
P	Polarization (C/m^2)
$\overline{P}$	Polarization kernel (C/m^2)
P^α	Polarization of α-variant (C/m^2)
P_R^α	Remanent polarization of α-variant (C/m^2)
P_m^α	Minimum polarization of α-variant (C/m^2)
s_α^E	Elastic compliance of α-variant at constant field (m^2/N)
T	Temperature (K)
x_+, x_-, x_{90}	Fraction of positively, negatively and 90° oriented dipoles (Unitless)
Y_α^P	Elastic stiffness of α-variant at constant polarization (N/m^2)
ϵ	Permittivity (F/m = C/Vm)
ε	Strain (Unitless)
$\overline{\varepsilon}$	Strain kernel
ε^α	Strain of α-variant
ε_R^α	Remanence strain of α-variant
ε_m^α	Minimum strain of α-variant
η^ε	Inverse susceptibility at constant strain (m/F = Vm/C)
σ	Stress (N/m^2)
τ_{90}	Relaxation time for 90° switching (s)
τ_{180}	Relaxation time for 180° switching (s)
χ_e	Electric susceptibility (Unitless)
χ_α^σ	Ferroelectric susceptibility of α-variant at constant stress (F/m = C/Vm)
ψ_α	Helmholtz energy density of α-variant (CV/m^3)

1 Introduction

Ferroelectric materials, such as lead zirconate titanate (PZT), lanthanum-doped lead zirconate titanate (PLZT), lead manganese niobate (PMN), polyvinylidene flouride (PVDF), and barium titanate (BaTiO$_3$), are being widely considered as actuators, sensors, and structural units for a range of aerospace, aeronautic, automotive, industrial and biomedical applications. Their advantages derive from the intrinsic properties of the materials. The complementary direct and converse piezoelectric effects imbue the materials with multiple design properties including sensor, actuator, self-monitoring and nondestructive evaluation, and energy harvesting capabilities. Their functionality is augmented by their solid state nature which promotes miniaturization and simplified design and reduces power requirements and heat generated by the units. Furthermore, ferroelectric actuators can provide nanometer positioning resolution and can operate at frequencies ranging from DC to MHz. As detailed in the companion paper [19], ferroelectric transducers are being considered, or are already being employed, for a large number of applications including high speed valves for fuel injectors, ferroelectric memory technologies (e.g., FeRAM), nanopositioning units (e.g., AFM and STM stages),

high speed camera shutters and autofocusing units, ultrasonic transducers for biomedical imaging and treatment, micro and pico air vehicle design, and energy harvesting devices.

However, the ferroelectric properties that imbue the materials with unique transducer capabilities also produce rate-dependent hysteresis, creep, and constitutive nonlinearities as illustrated in Figure 1. The field-polarization and field-strain data from [26] illustrates that rate-dependent effects are significant at frequencies as low as 1 Hz. PZT data from [24] illustrates that for fixed field inputs, both the strain and polarization exhibit significant creep on timescales of 1 to 20 seconds. Finally, the MFC data from [8] illustrates nested minor loop behavior typical of moderate drive regimes. Whereas the full switching behavior shown in Figure 1(a)-(e) will typically not be encountered in applications, general models must account for the full range of rate-dependent and creep behavior to provide comprehensive device characterization.

To be optimally utilized in applications, constitutive models must satisfy the following criteria: (i) they must adequately quantify the range of rate-dependent behavior exhibited by the materials, (ii) they must be in a form that can be readily extended to provided distributed models, for complex structures and devices, that are amenable to finite element implementation, (iii) they must be efficient to implement, (iv) they must be readily calibrated for a specific material or device, and (v) models employed in control designs can prove advantageous if they admit the construction of approximate inverse relations.

It is shown in [18–21] that the homogenized energy model (HEM) satisfies (i) and (ii). Furthermore, the construction of approximate inverses for previous formulations of the framework are reported in [4,18] and inversion techniques for the present formulation [19] are addressed in [15]. In this paper, we address (iii) and (iv) by presenting highly efficient implementation techniques and data-driven parameter estimation algorithms for the homogenized energy model. In combination, this
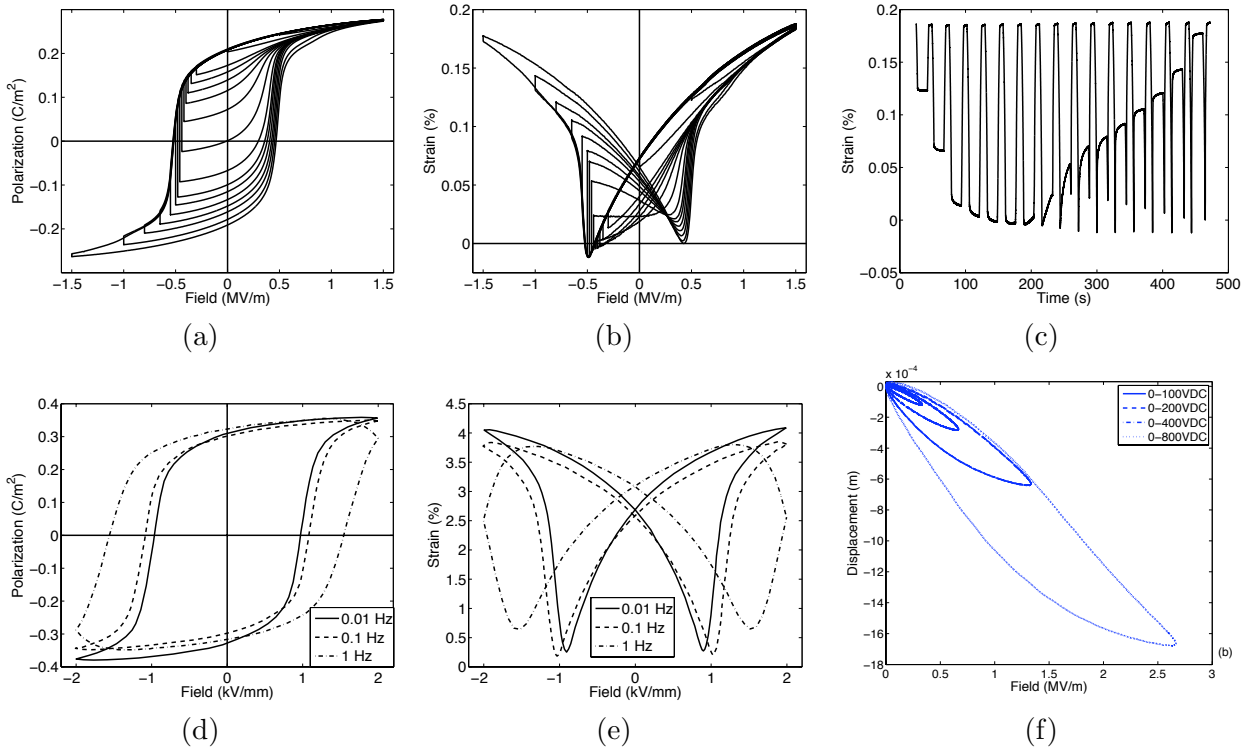

Figure 1: (a) Field-polarization, (b) field-strain and (c) time-strain PZT data from [24]. Rate-dependent (d) polarization and (e) strain PZT data from [26]. (f) Field-strain MFC data from [8].

2

provides the framework with significant flexibility for use in simulation packages, design algorithms, and control designs for systems utilizing ferroelectric transducers.

To provide context for the framework, we first summarize the mechanisms that produce the hysteretic behavior shown in Figure 1. The creep and rate-dependencies are due to the fact that kinetics associated with dipole switching typically differ from mechanical or electrical loading rates. Furthermore, it is discussed in [19] that the 180° switching associated with large polarization changes often occurs at a different rate than 90° switching associated with large strain changes. In combination, this establishes that multiple time scales must be incorporated in dynamic models.

As illustrated for a PZT-based macro-fiber composite (MFC) in Figure 2, hysteresis also involves multiple spatial scales. Within a domain, strains or changes in polarization are due to stress-induced material deformations or field-induced ion movement and the behavior is often reversible and linear. Field or stress-induced dipole switching at the grain level produces irreversible hysteresis in both the field-polarization and field-strain relations. For single crystal materials comprised of a single grain, the switching is typically rapid thus producing sharp hysteresis and butterfly loops in quasistatic operating regimes. For polycrystalline materials with distributed interaction and coercive fields, hysteresis and butterfly loops are smoothed due to nonuniform grain contributions. The behavior of hysteresis loops is further modified when hysteretic actuator or sensor materials are employed on distributed structures.
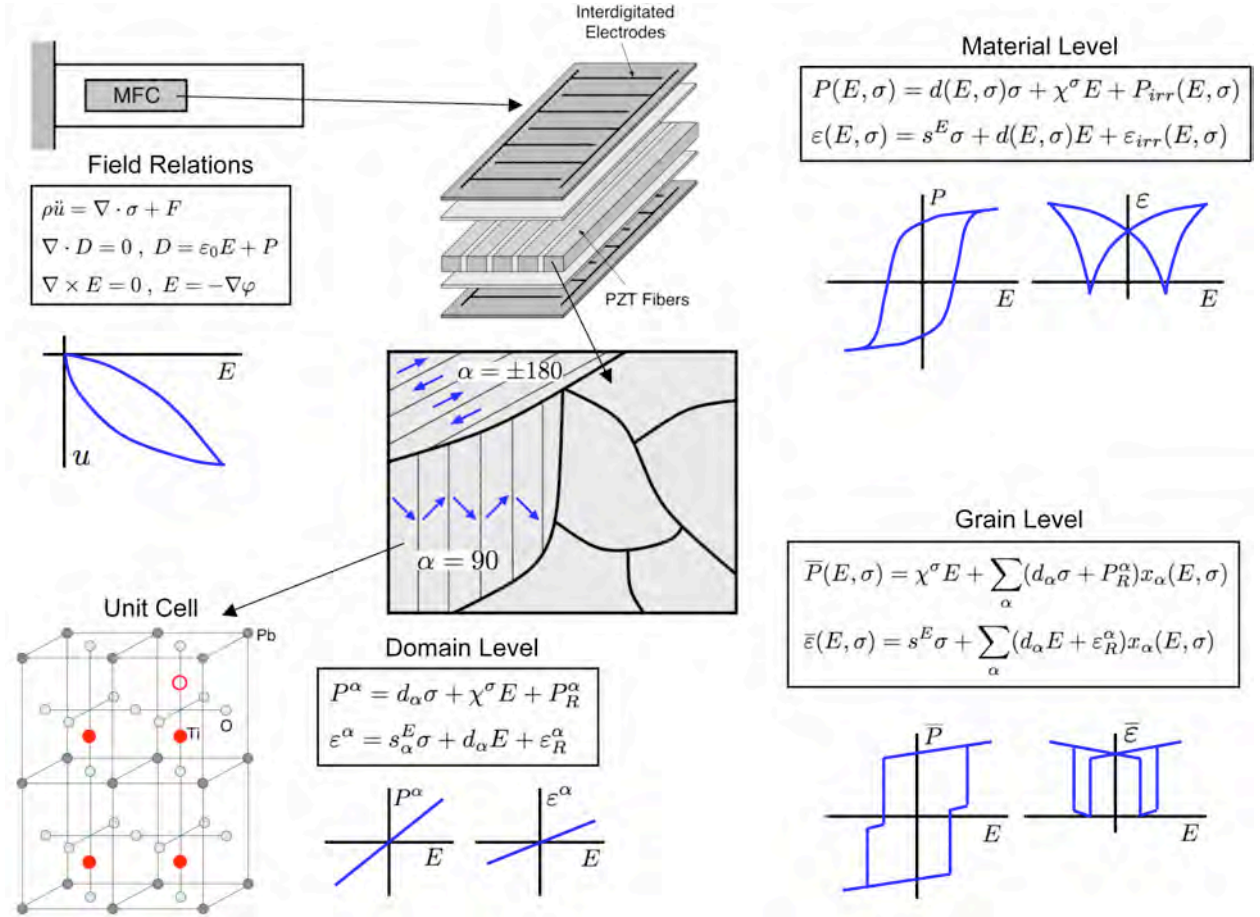

Figure 2: Multiscale behavior of a PZT-based MFC transducer at the application, device, material and unit cell levels.

As noted in Figure 2, material-level constitutive relations for the polarization P and strain ε can generically be expressed as

$$P(E,\sigma) = d(E,\sigma)\sigma + \chi^\sigma E + P_{irr}(E,\sigma)$$

$$\varepsilon(E,\sigma) = s^E \sigma + d(E,\sigma)E + \varepsilon_{irr}(E,\sigma)$$

where E, σ are input fields and stresses, χ^σ is the ferroelectric susceptibility at constant stress, s^E is the elastic compliance at constant field, and d is a piezoelectric coupling coefficient. We note that $d(E,\sigma), P_{irr}(E,\sigma)$ and $\varepsilon_{irr}(E,\sigma)$ incorporate the nonlinear and irreversible history-dependence due to dipole switching.

Various modeling hierarchies can be defined by the manner in which d, P_{irr} and ε_{irr} are constructed. Micromechanical, or microscopically-motivated models are based on an energy description of the material at the domain or grain level in combination with various homogenization techniques to provide expressions for the nonlinear, effective components d, P_{irr} and ε_{irr}. Phenomenological models circumvent the difficulties associated with quantifying complex, or poorly understood, micro-scale physics by constructing relations for d, P_{irr} and ε_{irr} based on macroscale observations or experimental measurements, often guided by thermodynamic constraints. Details regarding various models for ferroelectric materials can be found in [2, 9, 13, 16, 18, 19].

The homogenized energy model is a multiscale, micromechanical approach that begins with energy analysis at the domain level to construct the linear relations shown in Figure 2 for P^α and ε^α where α designates the dipole variant; e.g., $\alpha = \pm 180, 90$ for tetragonal materials. Switching processes due to domain wall nucleation and movement are incorporated by tracking the evolution of dipole fractions x_α which serve as internal variables. Differential equations quantifying the dynamics of x_α are driven by likelihood rates constructed using Boltzmann theory to quantify the scaled probability of transitioning between stable equilibria associated with dipole variants. This incorporates the rate-dependence and multiple-time scales exhibited by the data in Figure 1 and yields grain-level or single crystal kernels $\overline{P}$ and $\overline{\varepsilon}$. For polycrystalline materials, material-level models are constructed by assuming that properties such as coercive fields, critical driving forces, and interaction fields are manifestations of underlying densities rather than constants.

The three primary issues that must be addressed to construct implementation algorithms are: (i) efficient approximation of the integrals, posed on infinite and semi-infinite domains, arising in the homogenization step used to construct the irreversible components $d(E,\sigma), P_{irr}(E,\sigma)$ and $\varepsilon_{irr}(E,\sigma)$, (ii) efficient approximation of the evolution equations for x_α, and (iii) efficient evaluation of the likelihoods which incorporate rate-dependent effects and drive the evolution equations. The first issue is addressed by employing density representations that admit efficient numerical approximation on finite domains whereas implicit Euler discretizations readily address the second issue. The repeated evaluation of likelihoods is avoided by constructing arrays that permit high-speed access during model implementation. In combination, the evaluation of $d(E,\sigma), P_{irr}(E,\sigma)$ and $\varepsilon_{irr}(E,\sigma)$ are reduced to operations solely involving componentwise matrix multiplication and summation. Hence the operations are highly efficient and inherently parallelizable which facilitates subsequent implementation using devices such as field programmable gate arrays (FPGA) [3].

We note that approximate model inversion techniques rely on forward solutions of the model. Hence the efficiency of forward algorithms also directly contributes to the speed of inverse algorithms.

There are two primary issues that must be addressed when employing gradient-based optimization algorithms for the parameter estimation required for model calibration: (i) determination of accurate initial parameter estimates and (ii) efficient and accurate construction of gradients or Jacobians. Due to its physical nature, parameters in the homogenized energy model can be directly correlated with properties of measured data. We utilize that here to construct data-driven algorithms to determine

initial parameter estimates. Secondly, we construct analytic Jacobian relations which significantly improves both the speed and accuracy of optimization routines. In combination, this helps mitigate some of the difficulties associated with the shallow slopes and nonconvexity (multiple local minima) inherent to functionals employed in parameter estimation problems of this type.

We note that various aspects of the implementation and data-driven parameter estimation algorithms can be optimized to provide improved performance for specific data sets. Instead, our goal was to provide algorithms that balance simplicity, robustness, accuracy, and optimality for a wide range of materials, applications and operating regimes. Points were algorithms can be modified or optimized are noted in the discussion.

Following a brief summary of the model in Section 2, highly efficient implementation algorithms are presented in Section 3. The parameter estimation problem is discussed in Section 4 where we provide algorithms to construct analytic Jacobians and data-driven techniques to determine initial parameter estimates. Model calibration and validation are illustrated in Section 5 using PZT data from [24] and single crystal $BaTiO_3$ data from [5]. Additional examples illustrating the capability of the model to characterize creep and rate-dependent data, such as the shown in Figure 1, are provided in the companion paper [19] which details the model development.

2 Polarization and Strain Models

As detailed in [19], consideration of 180° dipole switching yields a macroscopic model quantifying the nonlinear and hysteretic field-polarization map for ferroelectric materials whereas the additional incorporation of 90° switching yields a homogenized model quantifying both the polarization and strains due to input fields and stresses. We summarize the latter model and indicate simplifications that occur if considering only the polarization in the absence of applied stresses.

Polarization and Strain Model

At the lattice level, we consider the Helmholtz and Gibbs energy densities

$$\psi_\alpha(P,\varepsilon) = \frac{1}{2}\eta_\alpha^\varepsilon(P - P_R^\alpha)^2 + \frac{1}{2}Y_\alpha^P(\varepsilon - \varepsilon_R^\alpha)^2 + h_\alpha(P - P_R^\alpha)(\varepsilon - \varepsilon_R^\alpha)$$

and

$$G_\alpha(E,\sigma;P,\varepsilon) = \psi_\alpha(P,\varepsilon) - EP - \sigma\varepsilon$$

where we indicate $\pm 180^o$ and 90° orientations by $\alpha = \pm, 90$. As summarized in the nomenclature table at the beginning of the paper, $P_R^\alpha, \varepsilon_R^\alpha, \eta_\alpha^\varepsilon, Y_\alpha^P$ and h_α denote the remanence polarization, remanence strain, inverse susceptibility at constant strain, elastic stiffness at constant polarization, and piezoelectric constant.

For a fixed applied field and stress, the conditions $\frac{\partial G}{\partial P} = 0$ and $\frac{\partial G}{\partial \varepsilon} = 0$ yield the relations

$$\begin{aligned} P_m^\alpha &= P_R^\alpha + \chi_\alpha^\sigma E + d_\alpha\sigma \\ \varepsilon_m^\alpha &= \varepsilon_R^\alpha + d_\alpha E + s_\alpha^E\sigma \end{aligned} \tag{1}$$

where

$$\chi_\alpha^\sigma = \frac{Y_\alpha^P}{Y_\alpha^P\eta_\alpha^\varepsilon - h_\alpha^2} \ , \ d_\alpha = \frac{h_\alpha}{h_\alpha^2 - Y_\alpha^P\eta_\alpha^\varepsilon} \ , \ s_\alpha^E = \frac{\eta_\alpha^\varepsilon}{Y_\alpha^P\eta_\alpha^\varepsilon - h_\alpha^2}$$

are the ferroelectric susceptibility at constant stress, the piezoelectric constant, and elastic compliance at constant field. The minimum of the Gibbs energy in each α-well can then be expressed as

$$G_{\alpha m}(E,\sigma) = -\frac{1}{2}\chi_\alpha^\sigma E^2 - \frac{1}{2}s_\alpha^E\sigma^2 - d_\alpha E\sigma - EP_R^\alpha - \sigma\varepsilon_R^\alpha.$$

5

The dipole fractions x_+, x_- and x_{90} associated with positively, negatively, and 90° degree dipoles evolve according to the differential equations

$$\dot{x}_- = -(p_{-90} + p_{-+})x_- + p_{90-}x_{90} + p_{+-}x_+$$

$$\dot{x}_{90} = p_{-90}x_- - (p_{90-} + p_{90+})x_{90} + p_{+90}x_+ \tag{2}$$

$$\dot{x}_+ = p_{-+}x_- + p_{90+}x_{90} - (p_{+90} + p_{+-})x_+$$

where

$$p_{\alpha\beta}(E, \sigma) = \frac{1}{\tau_{\alpha\beta}}e^{-\Delta G^a_{\alpha\beta}(E,\sigma)V/kT} \tag{3}$$

quantifies the likelihood of transitioning from an α-well to a β-well. As noted in Table 1, (2) can be simplified using the relation $x_+ + x_- + x_{90} = 1$. The activation energy is specified by the relation

$$\Delta G^a_{\alpha\beta}(E, \sigma; F_c) = \begin{cases} \Delta G_0(1 - F_{\alpha\beta}(E,\sigma)/F_c)^2 & , \quad F_{\alpha\beta}(E,\sigma) \leq F_c \\ 0 & , \quad F_{\alpha\beta}(E,\sigma) > F_c. \end{cases}$$

Here $F_{\alpha\beta}(E,\sigma) = G_{\alpha m}(E,\sigma) - G_{\beta m}(E,\sigma)$ is the thermodynamic driving force. The specific form of $F_{\alpha\beta}$, based on the physical assumption that

$$\chi^\sigma_+ = \chi^\sigma_- = \chi^\sigma_{90} = \chi^\sigma$$

$$s^E_+ = s^E_- = s^E_{90} = s^E$$

$$P^{90}_R = 0, P^+_R = -P^-_R, \varepsilon^+_R = \varepsilon^-_R \tag{4}$$

$$d_{90} = 0, d_- = -d_+$$

$$\tau_{90-} = \tau_{-90} = \tau_{90+} = \tau_{+90} = \tau_{90} \ , \ \tau_{+-} = \tau_{-+} = \tau_{180},$$

is given in Table 1. Note that

$$\Delta G_0 = \begin{cases} \frac{1}{4}F_c & , \quad 180^o \text{ Switching} \\ \frac{1}{16}F_c & , \quad 90^o \text{ Switching} \end{cases}$$

is the energy barrier at zero driving force.

The polarization and strain kernels are given by

$$\overline{P} = \sum_{\alpha=\pm,90} x_\alpha P^\alpha_m \quad , \quad \overline{\varepsilon} = \sum_{\alpha=\pm,90} x_\alpha \varepsilon^\alpha_m.$$

Based on (1) and (4), these relations can be expressed as

$$\overline{P}(E, \sigma) = \bar{d}(E,\sigma)\sigma + \chi^\sigma E + \overline{P}_{irr}(E,\sigma)$$

$$\overline{\varepsilon}(E, \sigma) = s^E \sigma + \bar{d}(E,\sigma)E + \overline{\varepsilon}_{irr}(E,\sigma)$$

where

$$\bar{d}(E, \sigma) = \sum_{\alpha=\pm,90} d_\alpha x_\alpha(E,\sigma)$$

$$\overline{P}_{irr}(E, \sigma) = \sum_{\alpha=\pm,90} P^\alpha_R x_\alpha(E,\sigma)$$

$$\overline{\varepsilon}_{irr}(E, \sigma) = \sum_{\alpha=\pm,90} \varepsilon^\alpha_R x_\alpha(E,\sigma).$$

6

In the final step in the development of [19], macroscopic models

$$P(E(t), \sigma(t); x_+^0) = \int_0^\infty \int_{-\infty}^\infty \overline{P}(E(t) + E_I, \sigma(t); F_c)\nu_I(E_I)\nu_c(F_c)dE_IdF_c$$

$$\varepsilon(E(t), \sigma(t); x_+^0) = \int_0^\infty \int_{-\infty}^\infty \overline{\varepsilon}(E(t) + E_I, \sigma(t); F_c)\nu_I(E_I)\nu_c(F_c)dE_IdF_c$$

are constructed by considering interaction fields E_I and thermodynamic driving forces F_c to be manifestations of underlying densities ν_I and ν_c. The final models can thus be expressed as

$$P(E, \sigma) = d(E, \sigma)\sigma + \chi^\sigma E + P_{irr}(E, \sigma)$$

$$\varepsilon(E, \sigma) = s^E \sigma + d(E, \sigma)E + \varepsilon_{irr}(E, \sigma)$$

where

$$d(E, \sigma) = \int_0^\infty \int_{-\infty}^\infty \bar{d}(E_e; F_c)\nu_I(E_I)\nu_c(F_c)dE_IdF_c$$

$$P_{irr}(E, \sigma) = \int_0^\infty \int_{-\infty}^\infty \overline{P}_{irr}(E_e; F_c)\nu_I(E_I)\nu_c(F_c)dE_IdF_c$$

$$\varepsilon_{irr}(E, \sigma) = \int_0^\infty \int_{-\infty}^\infty \overline{\varepsilon}_{irr}(E_e; F_c)\nu_I(E_I)\nu_c(F_c)dE_IdF_c.$$

Here $E_e(t) = E(t) + E_I$ is the effective field.

Details regarding various choices for the densities are provided in [19]. For the implementation and parameter estimation algorithms detailed in this paper, we employ the representations

$$\nu_c(F_c) = \frac{1}{\sum_\ell \alpha_\ell} \sum_{k=k_\alpha}^{K_\alpha} \alpha_k\phi_k(F_c) \quad , \quad \phi_k(F_c) = \frac{1}{\sigma_c^k F_c \sqrt{2\pi}}e^{-[\ln(F_c)-\ln(\bar{F}_c)]^2/2(\sigma_c^k)^2} \quad , \quad \sigma_c^k = 2^k\sigma_c$$

$$\nu_I(E_I) = \frac{1}{\sum_\ell \beta_\ell} \sum_{k=k_\beta}^{K_\beta} \beta_k\varphi_k(E_I) \quad , \quad \varphi_k(E_I) = \frac{1}{\sigma_I^k\sqrt{2\pi}}e^{-E_I^2/2(\sigma_I^k)^2} \qquad , \quad \sigma_I^k = 2^k\sigma_I$$

(5)

where the preceding sums ensure integration to unity. During model calibration, the parameters $\{\alpha_k, \beta_k\}$ are determined through a least squares fit to the data.

The complete polarization and strain model is summarized in Table 1.

Parameters for the Polarization-Strain Model

To construct the density basis functions $\varphi_k(E_I)$ and $\phi_k(F_c)$, it is necessary to determine values for the driving force mean $\mu_c = \ln(\bar{F}_c)$ and variance σ_c^2 as well as the interaction field variance σ_I^2. We denote this set of parameters by

$$\bar{p} = [\mu_c, \sigma_c^2, \sigma_I^2]. \tag{6}$$

We provide an algorithm in Section 4.2 to estimate values for these parameters based on measured attributes of E-P data. We note that these parameters are not updated or optimized through a least squares fit to data.

Based on the assumption (4), the remaining parameters are denoted by

$$p = [P_R^+, \varepsilon_R^+, \varepsilon_R^{90}, \chi^\sigma, d_+, s^E, \gamma, \tau_{90}, \tau_{180}, \alpha_k, \beta_k]. \tag{7}$$

This comprises the set that is optimized during model calibration.

Homogenized Energy Model:

$$P(E,\sigma) = d(E,\sigma)\sigma + \chi^\sigma E + P_{irr}(E,\sigma)$$

$$\varepsilon(E,\sigma) = s^E \sigma + d(E,\sigma)E + \varepsilon_{irr}(E,\sigma)$$

(8)

where

$$d(E,\sigma) = \int_0^\infty \int_{-\infty}^\infty \bar{d}(E+E_I;F_c)\nu_I(E_I)\nu_c(F_c)dE_I dF_c$$

$$P_{irr}(E,\sigma) = \int_0^\infty \int_{-\infty}^\infty \bar{P}_{irr}(E+E_I;F_c)\nu_I(E_I)\nu_c(F_c)dE_I dF_c$$

$$\varepsilon_{irr}(E,\sigma) = \int_0^\infty \int_{-\infty}^\infty \bar{\varepsilon}_{irr}(E+E_I;F_c)\nu_I(E_I)\nu_c(F_c)dE_I dF_c$$

(9)

Kernels:

$$\bar{d}(E,\sigma;F_c) = \sum_{\alpha=\pm,90} d_\alpha x_\alpha(E;F_c)$$

$$\bar{P}_{irr}(E,\sigma;F_c) = \sum_{\alpha=\pm,90} P_R^\alpha x_\alpha(E;F_c)$$

$$\bar{\varepsilon}_{irr}(E,\sigma;F_c) = \sum_{\alpha=\pm,90} \varepsilon_R^\alpha x_\alpha(E;F_c)$$

(10)

Evolution Equations: $(t;E,\sigma,F_c)$

$$\dot{x}_- = -(p_{-90}+p_{-+}+p_{90-})x_- + (p_{+-}-p_{90-})x_+ + p_{90-}$$

$$\dot{x}_+ = (p_{-+}-p_{90+})x_- - (p_{+90}+p_{+-}+p_{90+})x_+ + p_{90+}$$

$$x_{90} = 1 - x_+ - x_-$$

(11)

Likelihoods: $\alpha,\beta = \pm 90$

$$p_{\alpha\beta}(E,\sigma;F_c) = \frac{1}{\tau_{\alpha\beta}}e^{-\gamma \Delta G_{\alpha\beta}^a(E,\sigma;F_c)} \;\;,\;\; \gamma = V/kT$$

(12)

Activation Energy: $\alpha,\beta = \pm 90$

$$\Delta G_{\alpha\beta}^a(E,\sigma;F_c) = \begin{cases} \Delta G_0(1-F_{\alpha\beta}(E,\sigma)/F_c)^2 & , \;\; F_{\alpha\beta}(E,\sigma) \leq F_c \\ 0 & , \;\; F_{\alpha\beta}(E,\sigma) > F_c \end{cases}$$

$$F_{90+}(E,\sigma) = d_+ E\sigma + P_R^+ E - (\varepsilon_R^{90}-\varepsilon_R^+)\sigma \;\;\;\;, \;\; F_{+90} = -F_{90+}$$

$$F_{90-}(E,\sigma) = -d_+ E\sigma - P_R^+ E - (\varepsilon_R^{90}-\varepsilon_R^+)\sigma \;\;, \;\; F_{-90} = -F_{90-}$$

$$F_{+-}(E,\sigma) = -2d_+ E\sigma - 2EP_R^+ \;\;\;\;\;\;\;\;\;\;\;\;\;\;\;\;, \;\; F_{-+} = -F_{+-}$$

(13)

Densities:

$$\nu_c(F_c) = \frac{1}{\sum_\ell \alpha_\ell}\sum_{k=k_\alpha}^{K_\alpha} \alpha_k \phi_k(F_c) \;\;\;\;, \;\; \phi_k(F_c) = \frac{1}{\sigma_c^k F_c \sqrt{2\pi}}e^{-[\ln(F_c)-\ln(\bar{F}_c)]^2/2(\sigma_c^k)^2}$$

$$\nu_I(E_I) = \frac{1}{\sum_\ell \beta_\ell}\sum_{k=k_\beta}^{K_\beta} \beta_k \varphi_k(E_I) \;\;\;\;, \;\; \varphi_k(E_I) = \frac{1}{\sigma_I^k \sqrt{2\pi}}e^{-E_I^2/2(\sigma_I^k)^2}$$

(14)

Table 1: Components of the polarization and strain model based on 90° dipole switching.

Polarization Model

If solely quantifying the polarization in the absence of applied stresses, one can consider energy landscapes and dipole fractions associated only with positively and negatively oriented dipoles which we designate by $\alpha = \pm$. It is shown in [19] that a complete characterization of the Helmholtz and Gibbs energy densities yields likelihoods p_{-+} and p_{+-} formulated in terms of complementary error functions whereas formulation in terms of the activation energy yields likelihood relations analogous to (3). We focus on this latter case and note that analogous implementation and parameter estimation algorithms can be constructed for the error function formulation.

The polarization model based on 180° dipole switching is summarized in Table 2.

Polarization Model Parameters

In this case, we employ a coercive field density $\nu_c(E_c)$ having the same form as the driving force density $\nu_c(F_c)$. Hence it is again necessary to prescribe data-driven algorithms to determine values of the coefficients $\bar{p}$ in (6). The parameters to be estimated through a least squares fit to data are

$$p = [\eta, P_R, \gamma, \tau, \alpha_k, \beta_k]. \tag{15}$$

We discuss associated optimization algorithms in Section 4 and data-driven techniques to obtain initial parameter estimates in Section 4.2.

3   Implementation Algorithms

To facilitate implementation of the models summarized in Tables 1 and 2, or their inverses, three issues must be addressed: (i) approximation of the infinite-domain integrals in a manner that retains its accuracy for the basis expansions (5), (ii) evaluations of the likelihoods $p_{\alpha\beta}$ in an efficient manner, and (iii) efficient solution of the differential equations (11) and (19).

3.1   Quadrature Techniques

To implement the model, the integrals defining the terms d, P_{irr} and ε_{irr} in (9) and (17) must be approximated in a manner that is both efficient and accurate. We first note that by employing the relations (10), these terms can be expressed as

$$d(E, \sigma) = \sum_{\alpha=\pm,90} d_\alpha \int_0^\infty \int_{-\infty}^\infty x_\alpha(E_e; F_c)\nu_I(E_I)\nu_c(F_c)dE_I dF_c$$

$$P_{irr}(E, \sigma) = \sum_{\alpha=\pm,90} P_R^\alpha \int_0^\infty \int_{-\infty}^\infty x_\alpha(E_e; F_c)\nu_I(E_I)\nu_c(F_c)dE_I dF_c$$

$$\varepsilon_{irr}(E, \sigma) = \sum_{\alpha=\pm,90} \varepsilon_R^\alpha \int_0^\infty \int_{-\infty}^\infty x_\alpha(E_e; F_c)\nu_I(E_I)\nu_c(F_c)dE_I dF_c.$$

Secondly, it is noted in [19] that the densities satisfy exponential decay constraints. Hence approximation algorithms can be defined on finite domains rather than necessitating quadrature techniques for infinite and semi-infinite domains. We illustrate here a trapezoidal formula and refer the reader to [18] for details regarding composite Gaussian quadrature techniques. We note that truncation of the domains and use of composite techniques is more efficient to implement than Gauss-Hermite and Gauss-Laguerre algorithms, that are designed specifically for infinite and semi-infinite intervals,

Homogenized Energy Model:

$$P(E) = \frac{E}{\eta} + P_{irr} \tag{16}$$

where

$$P_{irr}(E) = \int_0^\infty \int_{-\infty}^\infty \bar{P}_{irr}(E + E_I; F_c)\nu_I(E_I)\nu_c(F_c)dE_I dF_c \tag{17}$$

Kernel:

$$\bar{P}_{irr}(E; F_c) = \sum_{\alpha=\pm 90} P_R^\alpha x_\alpha(E; F_c) = -P_R + 2P_R x_+ \tag{18}$$

Evolution Equations: $(t, E; F_c)$

$$\dot{x}_+ = -(p_{-+} + p_{+-})x_+ + p_{-+}$$
$$x_- = 1 - x_+ \tag{19}$$

Likelihoods (Choice 1): $\alpha, \beta = \pm$

$$p_{\alpha\beta}(E; F_c) = \frac{1}{\tau}e^{-\gamma \Delta G_{\alpha\beta}^a(E; F_c)} \ , \ \gamma = V/kT \tag{20}$$

Activation Energy: $\alpha, \beta = \pm 90, F_c = 2E_c P_R, \Delta G_0 = \frac{F_c}{4}$

$$\Delta G_{\alpha\beta}^a(E; F_c) = \begin{cases} \Delta G_0(1 - F_{\alpha\beta}(E)/F_c)^2 & , & F_{\alpha\beta}(E) \leq F_c \\ 0 & , & F_{\alpha\beta}(E) > F_c \end{cases} \tag{21}$$

$$F_{-+}(E) = 2EP_R \quad , \quad F_{+-} = -F_{-+}$$

Likelihoods (Choice 2):

$$p_{+-}(E; E_c) = \frac{\gamma_1}{\text{erfcx}[\gamma_2(-E - E_c)]} \ , \ p_{-+}(E; E_c) = \frac{\gamma_1}{\text{erfcx}[\gamma_2(E - E_c)]} \tag{22}$$

where

$$\gamma_1 = \frac{1}{\tau}\sqrt{\frac{2V\eta}{\pi kT}} \quad , \quad \gamma_2 = \sqrt{\frac{V}{2kT\eta}}$$

Densities:

$$\nu_c(F_c) = \frac{1}{\sum_\ell \alpha_\ell} \sum_{k=k_\alpha}^{K_\alpha} \alpha_k \phi_k(F_c) \quad , \quad \phi_k(F_c) = \frac{1}{\sigma_c^k F_c \sqrt{2\pi}} e^{-[\ln(F_c)-\ln(\bar{F}_c)]^2/2(\sigma_c^k)^2}$$

$$\nu_I(E_I) = \frac{1}{\sum_\ell \beta_\ell} \sum_{k=k_\beta}^{K_\beta} \beta_k \varphi_k(E_I) \quad , \quad \varphi_k(E_I) = \frac{1}{\sigma_I^k \sqrt{2\pi}} e^{-E_I^2/2(\sigma_I^k)^2} \tag{23}$$

Table 2: Components of the polarization model based on 180° dipole switching and the physical assumptions (4) with $P_R \equiv P_R^+$ and $\tau \equiv \tau_{180}$.

because they allow accurate evaluation of the density expansions (5) and construction of lookup tables to improve algorithm efficiency as detailed in Section 3.2.

If we let F_{c_i}, E_{I_j} and v_i, w_j respectively denote the quadrature points and weights, we obtain the approximate relations

$$\int_0^\infty \int_{-\infty}^\infty x_\alpha(E + E_I; F_c)\nu_I(E_I)\nu_c(F_c)dE_I dF_c \approx \sum_{i=1}^{N_i}\sum_{j=1}^{N_j} x_\alpha(E + E_{I_j}; F_{c_i})\nu_I(E_{I_j})\nu_c(F_{c_j})v_i w_j. \quad (24)$$

For the validation results reported in Section 5, sufficient accuracy was achieved using a trapezoid rule with $N_i = N_j = 41$.

3.2 Determination of Phase Fractions and Likelihoods

From (24), it is observed that evaluation of the model requires the solution of $N_i \times N_j$ differential equations for each phase fraction x_α which in turn requires $N_i \times N_j$ evaluations of the likelihoods $p_{\alpha\beta}$. Due to its relative simplicity, we first illustrate a highly efficient implementation algorithm for the 180° polarization model. In Section 3.2.2, an analogous, but slightly more complicated, algorithm is developed for the 90° polarization-strain model.

3.2.1 Polarization Model

To approximate the solution of (19), it is shown in [4] that for sufficiently small stepsizes Δt, an implicit Euler discretization yields the stable difference relation

$$x_+^{k+1} = c_1^{k+1}x_+^k + c_2^{k+1}$$

where $t_k = k\Delta t$, $E_e^k = E_e(t_k) = E(t_k) + E_I$, $x_+^k = x_+(t_k; e_E^k, F_c)$ and

$$
\begin{aligned}
c_1^{k+1} &= \frac{1}{1 + \Delta t[p_{-+}(E_e^{k+1}; F_c) + p_{+-}(E_e^{k+1}; F_c)]} \\[2mm]
c_2^{k+1} &= \frac{p_{-+}(E_e^{k+1}; F_c)\Delta t}{1 + \Delta t[p_{-+}(E_e^{k+1}; F_c) + p_{+-}(E_e^{k+1}; F_c)]}.
\end{aligned}
\qquad (25)
$$

From (16) and (24), it follows that

$$P(E^k) = \frac{E^k}{\eta} - P_R + 2P_R V^T X_+^k W. \qquad (26)$$

where the vectors

$$
\begin{aligned}
V^T &= \left[v_1\nu_c(F_{c_1}), \; \cdots \;, v_{N_i}\nu_c(F_{c_{N_i}})\right]_{1\times N_i} \\[2mm]
W^T &= \left[w_1\nu_I(E_{I_1}), \; \cdots \;, w_{N_j}\nu_I(E_{I_{N_j}})\right]_{1\times N_j}
\end{aligned}
\qquad (27)
$$

incorporate the quadrature weights and densities evaluated at the quadrature points. The $N_i \times N_j$ matrix X_+^k quantifies the dipole orientations at the quadrature points and is defined as

$$
\begin{aligned}
\left[X_+^{k+1}\right]_{ij} &= x_+(t_{k+1}, E^{k+1} + E_{I_j}; F_{c_i}) \\[2mm]
&= \frac{x_+(t_k, E^k + E_{I_j}; F_{c_i})}{1 + \Delta t[p_{-+}(E^{k+1} + E_{I_j}; F_{c_j}) + p_{+-}(E^{k+1} + E_{I_j}; F_{c_j})]} \\[2mm]
&\quad + \frac{p_{-+}(E^{k+1} + E_{I_j}; F_{c_j})\Delta t}{1 + \Delta t[p_{-+}(E^{k+1} + E_{I_j}; F_{c_j}) + p_{+-}(E^{k+1} + E_{I_j}; F_{c_j})]}.
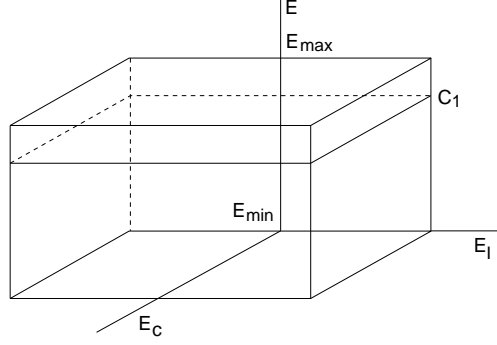\end{aligned}
\qquad (28)
$$

11

Figure 3: Structure of the 3-D array $\mathcal{C}_1$ and 2-D array C_1 for specified field value.

Remark 1. Because the constants c_1 and c_2 in (25) depend on field values but not explicitly on time, they can be evaluated offline and stored for highly efficient subsequent model implementation. To achieve this, one can construct 3-dimensional arrays $\mathcal{C}_1$ and $\mathcal{C}_2$ whose coordinates are F_c, E_I and E with values at the quadrature points (F_{c_i}, E_{I_j}) and field values E^ℓ uniformly distributed between minimum and maximum field values $E_{\min}, E_{\max}$ of operation; see Figure 3. During model execution — e.g., during parameter estimation or model-based control implementation — one would access the 2-dimensional, $N_i \times N_j$, arrays $C_1^\ell = \mathcal{C}_1(:,:,E^\ell)$ and $C_2^\ell = \mathcal{C}_2(:,:,E^\ell)$, for E^ℓ nearest the specified field value E^{k+1}, and update X_+ using the componentwise matrix multiplication and summation

$$X_+^{k+1} = C_1^\ell \cdot \times X^k + C_2^\ell.$$

When combined with (26), the efficiency of implementing the thermal relaxation model is the same as that of Algorithm 2.6.4 on page 117 of [18] for the negligible relaxation model.

An alternative is to form arrays $\mathcal{P}_{-+}, \mathcal{P}_{+-}$ storing the likelihoods at the $N_i \times N_j$ quadrature points and predefined field values. The matrices C_1^ℓ, C_2^ℓ can then be constructed using the operations defined in (28). This is slightly less efficient but can preferable if memory is limited and $\mathcal{P}_{-+}, \mathcal{P}_{+-}$ are used for the Jacobian construction described in Section 4. It is also advantageous if variable stepsizes Δt are required for control implementation.

3.2.2 Polarization-Strain Model

From (8)-(10), it follows that the discretized polarization and strain relations can be expressed as

$$P(E, \sigma) = \chi^\sigma E + \sum_{\alpha=\pm,90} (\sigma d_\alpha + P_R^\alpha) V^T X_\alpha(t; E, \sigma) W$$

$$\varepsilon(E, \sigma) = s^E \sigma + \sum_{\alpha=\pm,90} (E d_\alpha + \varepsilon_R^\alpha) V^T X_\alpha(t; E, \sigma) W \tag{29}$$

where V and W are defined in (27). The $N_i \times N_j$ matrices $X_\alpha(E, \sigma)$ are defined componentwise by

$$[X_\alpha(t; E, \sigma)]_{ij} = x_\alpha(t; E + E_{I_j}, \sigma, F_{c_i}) , \quad \alpha = \pm, 90 \tag{30}$$

where $x_{\pm,90}$ are solutions of (11).

For discrete time, field and stress values $t_k = k\Delta t, E^k = E(t_k)$ and $\sigma^k = \sigma(t_k)$, we let $x_\alpha^k = x_\alpha(t_k; E^k + E_I, \sigma^k, F_c)$ and $[X_\alpha^k]_{ij} = x_\alpha(t_k; E^k + E_{I_j}, \sigma^k, F_{c_i})$ denote the associated dipole fractions

12

and matrix of dipole fractions evaluated at quadrature points. An implicit Euler discretization then yields

$$a_{11}^{k+1} x_-^{k+1} + a_{12}^{k+1} x_+^{k+1} = x_-^k + a_{13}^{k+1}$$
$$a_{21}^{k+1} x_-^{k+1} + a_{22}^{k+1} x_+^{k+1} = x_+^k + a_{23}^{k+1}$$

(31)

where

$$a_{11}^{k+1} = 1 + \Delta t \left(p_{-90} + p_{-+} + p_{90-} \right) \quad , \quad a_{21}^{k+1} = -\Delta t (p_{-+} + p_{90+})$$
$$a_{12}^{k+1} = -\Delta t (p_{+-} + p_{90-}) \quad , \quad a_{22}^{k+1} = 1 + \Delta t \left(p_{+90} + p_{+-} + p_{90+} \right)$$
$$a_{13}^{k+1} = \Delta t p_{90-} \quad , \quad a_{23}^{k+1} = \Delta t p_{90+}.$$

We note that like the dipole fractions, these constants depend on (E, E_I, F_c); e.g., $a_{13}^{k+1}(E, E_I, F_c) = \Delta t p_{90-}(E^{k+1} + E_I; F_c)$.

Using Cramer's rule, one can solve (31) to obtain

$$x_-^{k+1} = c_1^{k+1} x_-^k + c_2^{k+1} x_+^k + c_3^{k+1}$$
$$x_+^{k+1} = d_1^{k+1} x_-^k + d_2^{k+1} x_+^k + d_3^{k+1}$$

where

$$c_1^{k+1} = \frac{a_{22}^{k+1}}{\det} \quad , \quad c_2^{k+1} = \frac{-a_{12}^{k+1}}{\det} \quad , \quad c_3^{k+1} = \frac{1}{\det} \left[a_{22}^{k+1} a_{13}^{k+1} - a_{12}^{k+1} a_{23}^{k+1} \right]$$

$$d_1^{k+1} = \frac{-a_{21}^{k+1}}{\det} \quad , \quad d_2^{k+1} = \frac{a_{11}^{k+1}}{\det} \quad , \quad d_3^{k+1} = \frac{1}{\det} \left[a_{11}^{k+1} a_{23}^{k+1} - a_{13}^{k+1} a_{21}^{k+1} \right]$$

$$\det = a_{11}^{k+1} a_{22}^{k+1} - a_{12}^{k+1} a_{21}^{k+1}.$$

To facilitate efficient implementation, we follow the strategy detailed in Remark 1 and construct 3-D arrays $\mathcal{C}_1$ - $\mathcal{D}_3$ comprised of the constants c_1 - d_3 evaluated at the quadrature points (F_{c_i}, E_{I_j}) and field values E^ℓ uniformly distributed between the minimum and maximum field values $E_{\min}$ and $E_{\max}$; e.g., $[\mathcal{C}_2]_{ij} = \Delta t [p_{+-}(E^\ell + E_{I_j}; F_{c_i}) + p_{90-}(E^\ell + E_{I_j}; F_{c_i})]/\det(E^\ell, E_{I_j}, F_{c_i})$. During model implementation, one then accesses the $N_i \times N_j$ matrices $C_1^\ell, C_2^\ell, C_3^\ell, D_1^\ell, D_2^\ell, D_3^\ell$, nearest to the specified field value E^k. The matrices of dipole fractions are then updated using the relation

$$X_+^{k+1} = C_1^\ell \cdot \times X_+^k + C_2^\ell \cdot \times X_-^k + C_3^\ell$$
$$X_-^{k+1} = D_1^\ell \cdot \times X_+^k + D_2^\ell \cdot \times X_-^k + D_3^\ell$$
$$X_{90}^{k+1} = I - X_+^{k+1} - X_-^{k+1}$$

which again involves only componentwise matrix multiplication and summation.

4 Parameter Estimation Problem

The data for the parameter estimation problem is taken to be either polarization measurements P_i or polarization-strain pairs $\{P_i, \varepsilon_i\}$ corresponding to N_d field values $E(t_i)$. The model response with parameters p for the same field values and a constant prestress σ_0 is denoted by $P(E(t_i), \sigma_0; p)$ and $\varepsilon(E(t_i), \sigma_0; p)$.

To calibrate the 180° polarization model, summarized in Table 2, with the parameter p given by (15), we minimize the functional

$$J(p) = \frac{1}{2} \sum_{i=1}^{N_d} e^2(t_i; p)$$

(32)

13

where
$$e(t_i; p) = P(E(t_i), \sigma_0; p) - P_i. \tag{33}$$

We first note that the magnitudes of the first four parameters $\{\eta, P_R, \gamma, \tau\}$ can vary from 10^{-4} to 10^8 so the performance of optimization algorithms is significantly improved by scaling the parameters by dividing by their magnitudes. To accomplish this, we form a vector s, whose components are the scale of each parameter, and minimize instead

$$J(q) = \frac{1}{2} \sum_{i=1}^{N_d} e^2(t_i; q. \times s) \tag{34}$$

where $q = p./s$ and $./$ and $.\times$ respectively denote componentwise division and multiplication. Because the components of q are on the order of unity, (34) is more readily mimimized using standard optimization software.

To estimate parameters for the combined polarization and strain model (8), we employ the functional

$$
\begin{aligned}
J(q) &= \frac{1}{2} \sum_{i=1}^{N_d} w_P e_P^2(t_i; q. \times s) + \frac{1}{2} \sum_{i=1}^{N_d} w_\varepsilon e_\varepsilon^2(t_i; q. \times s) \\
&= \frac{1}{2} \sum_{i=1}^{2N_d} R_i(q)
\end{aligned}
\tag{35}
$$

where

$$e_P(t_i; q. \times s) = P(E(t_i), \sigma_0; q. \times s) - P_i$$

$$e_\varepsilon(t_i; q. \times s) = \varepsilon(E(t_i), \sigma_0; q. \times s) - \varepsilon_i$$

$$R_i(q) = \begin{cases} w_P e_P^2(t_i; q. \times s) & , \quad i = 1, \cdots, N_d \\ w_\varepsilon e_\varepsilon^2(t_i; q. \times s) & , \quad i = N_d + 1, \cdots, 2N_d. \end{cases}$$

Here $p = q. \times s$ is given by (7). Since polarization is typically on the order of 10^{-1} and strain on the order of 10^{-3}, the weights w_P and w_ε are chosen to balance the polarization and strain components of (37).

The behavior of the functionals $J(q)$ is typical of those arising in parameter estimation problems; they have shallow slopes near the global minimum (if it exists) and they are typically nonconvex with multiple local minima.

One possibility is to employ stochastic optimization techniques such as genetic algorithms, simulated annealing, and differential evolution [22]. These techniques reduce the reliance on accurate initial parameter estimates and, in theory, provide global convergence. However, their convergence rates are slower — they may require infinite time for convergence — and, because they are nondeterministic, multiple optimizations can yield varying final parameter values.

Alternatively, one can employ gradient-based techniques such as the interior-reflective Newton, Levenberg-Marquardt, or sequential quadratic programming methods employed in the MATLAB routines `lsqnonlin` and `fmincon`. The efficiency and success of gradient-based optimization methods is predicated on determining good initial parameter estimates and being able to accurately determine gradients. We show next that analytic gradient expressions can be constructed for the homogenized energy model and, in Section 4.2, we use physical aspects of the model to develop data-driven techniques to provide initial parameter estimates based on measured properties of polarization and strain data. In combination, this permits routines, such as `lsqnonlin` which is used to optimize (32) and (33), to be implemented in a matter of minutes.

4.1 Analytic Jacobian or Gradient Relations

Most commercial optimization packages provide the option for constructing the Jacobian using finite difference approximation or providing an analytic expression. The former option is certainly feasible for optimizing (34) or (35) but it will be significantly slower and slightly less accurate than optimization using the analytic Jacobian. We illustrate first the computation of the Jacobian for the polarization model (16) with the functional (34) since it is simpler than that for the combined polarization-strain model.

Polarization Model

The Jacobian corresponding to (34) is

$$
\mathcal{J} = \begin{bmatrix}
\frac{\partial e(t_1;p)}{\partial \eta} & \frac{\partial e(t_1;p)}{\partial P_R} & \cdots & \frac{\partial e(t_1;p)}{\partial \beta_k} \\
\vdots & \vdots & & \vdots \\
\frac{\partial e(t_{N_d};p)}{\partial \eta} & \frac{\partial e(t_{N_d};p)}{\partial P_R} & \cdots & \frac{\partial e(t_{N_d};p)}{\partial \beta_k}
\end{bmatrix}
\tag{36}
$$

where $e(t_i; p)$ is defined in (33). We note that

$$
[\mathcal{J}]_{ij} = \frac{\partial e(t_i;p)}{\partial q_j} = \frac{\partial}{\partial q_j} P(E(t_i), \sigma_0; p) = \frac{\partial}{\partial p_j} P(E(t_i), \sigma_0; p) \frac{dp_j}{dq_j} = \frac{\partial}{\partial p_j} P(E(t_i), \sigma_0; p) s_j
\tag{37}
$$

so the Jacobian is simply the gradient or sensitivity of P with respect to the parameters. For the discretized model, these derivatives have the form

$$
\frac{\partial P}{\partial \eta} = -\frac{E}{\eta^2} \qquad , \qquad \frac{\partial P}{\partial P_R} = -1 + 2V^T[X_+]W + 2P_R V^T[\partial_{P_R} X_+]W
$$

$$
\frac{\partial P}{\partial \gamma} = 2P_R V^T[\partial_\gamma X_+]W \qquad , \qquad \frac{\partial P}{\partial \tau} = 2P_R V^T[\partial_\tau X_+]W
$$

$$
\frac{\partial P}{\partial \alpha_k} = \frac{2P_R}{\sum_\ell \alpha_\ell}(\mathcal{V}_k - V)^T[X_+]W \quad , \quad \frac{\partial P}{\partial \beta_k} = \frac{2P_R}{\sum_\ell \beta_\ell} V^T[X_+](\mathcal{W}_k - W)
$$

where $[V^T]_i = v_i \nu_c(F_{c_i}), [W]_j = w_j \nu_I(E_{I_j})$, as indicated in (27), and $[\mathcal{V}_k^T]_i = v_i \phi_k(F_{c_i}), [\mathcal{W}_k]_j = w_j \varphi_k(E_{I_j})$. The components of the $N_i \times N_j$ matrices $[\partial_\xi X_+]_{ij} = \frac{\partial x_+}{\partial \xi}(t; E(t) + E_{I_j}, \sigma_0; F_{c_i})$ for $\xi = P_R, \gamma, \tau$, can be found by differentiating the evolution equation (19) and switching the order of differentiation to obtain the differential equations

$$
\dot{x}^{P_R} = -(\partial_{P_R} p_{+-} + \partial_{P_R} p_{-+})\, x_+ - (p_{+-} + p_{-+})x^{P_R} + \partial_{P_R} p_{-+}
$$

$$
\dot{x}^\gamma = -(\partial_\gamma p_{+-} + \partial_\gamma p_{-+})\, x_+ - (p_{+-} + p_{-+})x^\gamma + \partial_\gamma p_{-+}
$$

$$
\dot{x}^\tau = -(\partial_\tau p_{+-} + \partial_\tau p_{-+})\, x_+ - (p_{+-} + p_{-+})x^\tau + \partial_\tau p_{-+}
$$

in the variables $x^{P_R} \equiv \frac{\partial x_+}{\partial P_R}, x^\gamma \equiv \frac{\partial x_+}{\partial \gamma}$ and $x^\tau \equiv \frac{\partial x_+}{\partial \tau}$ with

$$
\partial_{P_R} p_{+-} = \begin{cases} -\gamma \frac{(E+E_c)^2}{2E_c} p_{+-} & , \quad E \le E_c \\ 0 & , \quad E > E_c \end{cases} \quad , \quad \partial_{P_R} p_{-+} = \begin{cases} -\gamma \frac{(E-E_c)^2}{2E_c} p_{-+} & , \quad E \le E_c \\ 0 & , \quad E > E_c \end{cases}
$$

$$
\partial_\gamma p_{+-} = -\Delta G^a_{+-} p_{+-} \qquad\qquad , \quad \partial_\gamma p_{-+} = -\Delta G^a_{-+} p_{-+}
$$

$$
\partial_\tau p_{+-} = -\frac{1}{\tau} p_{+-} \qquad\qquad\qquad , \quad \partial_\tau p_{-+} = -\frac{1}{\tau} p_{-+}.
$$

$$\tag{38}$$

Given values of x_+ and x_-, the differential equations (36) can be solved using an implicit Euler method analogous to that described in Section 3.2.1 to approximate the solution of (19).

Remark 2. The Jacobian construction can be facilitated by the use of lookup tables, in a manner analogous to that described in Section 3.2.1, to avoid the repeated evaluation of the likelihoods p_{+-} and p_{-+} for all of the quadrature points (F_{c_i}, E_{I_j}). Alternatively, if memory is limited, one can construct two arrays $\mathcal{P}_{-+}, \mathcal{P}_{+-}$ storing the likelihoods at field values and quadrature points in a manner similar to that discussed in Remark 1 of Section 3. If memory is plentiful, it will be more efficient to construct lookup tables associated with the quantities defined in (38).

Polarization-Strain Model

The construction of the Jacobian for the functional (33) is analogous but slightly more complicated since it involves more parameters $p = [P_R^+, \varepsilon_R^+, \varepsilon_R^{90}, \chi^\sigma, d_+, s^E, \gamma, \tau_{90}, \tau_{180}, \alpha_k, \beta_k]$. We first note that the model (29) exhibits the parameter dependencies

$$P(E, \sigma) = \chi^\sigma E + \sum_{\alpha=\pm,90} (\sigma d_\alpha + P_R^\alpha) V^T(\alpha_k) X_\alpha(t; E, \sigma, \hat{p}) W(\beta_k)$$

$$\varepsilon(E, \sigma) = s^E \sigma + \sum_{\alpha=\pm,90} (E d_\alpha + \varepsilon_R^\alpha) V^T(\alpha_k) X_\alpha(t; E, \sigma, \hat{p}) W(\beta_k)$$

where V and W are defined in (27), X_α is defined in (30), and

$$\hat{p} = [P_R^+, \varepsilon_R^+, \varepsilon_R^{90}, d_+, \gamma, \tau_{90}, \tau_{180}].$$

With the assumptions(4) and definitions $[\mathcal{V}_k^T]_i = v_i \phi_k(F_{c_i})$, $[\mathcal{W}_k]_j = w_j \varphi_k(E_{I_j})$, it follows that

$$\frac{\partial P}{\partial P_R^+} = V^T[X_+]W - V^T[X_-]W + \sum_{\alpha=\pm,90} (\sigma d_\alpha + P_R^\alpha) V^T[\partial_{P_R^+} X_\alpha]W$$

$$\frac{\partial P}{\partial d_+} = \sigma V^T[X_+]W - \sigma V^T[X_-]W + \sum_{\alpha=\pm,90} (\sigma d_\alpha + P_R^\alpha) V^T[\partial_{d_+} X_\alpha]W$$

$$\frac{\partial P}{\partial \zeta} = \sum_{\alpha=\pm,90} (\sigma d_\alpha + P_R^\alpha) V^T[\partial_\zeta X_\alpha]W$$

$$\frac{\partial P}{\partial \alpha_k} = \sum_{\alpha=\pm,90} \frac{(\sigma d_\alpha + P_R^\alpha)}{\sum_\ell \alpha_\ell} (\mathcal{V} - V)^T[X_\alpha]W \quad , \quad \frac{\partial P}{\partial \beta_k} = \sum_{\alpha=\pm,90} \frac{(\sigma d_\alpha + P_R^\alpha)}{\sum_\ell \beta_\ell} V^T[X_\alpha](\mathcal{W} - W)$$

$$\frac{\partial P}{\partial \chi^\sigma} = E \quad , \quad \frac{\partial P}{\partial s^E} = 0$$

for $\zeta = \varepsilon_R^+, \varepsilon_R^{90}, \gamma, \tau_{90}$ and τ_{180}. Differentiation of the strain relations yields similar terms.

We next discuss the construction of the $N_i \times N_j$ matrices $[\partial_\xi X_\alpha]_{ij} = \frac{\partial x_\alpha}{\partial \xi}(t; E(t) + E_{I_j}, \sigma_0; F_{c_i})$ where $\xi = P_R^+, d_+, \varepsilon_R^+, \varepsilon_R^{90}, \gamma, \tau_{90}$ and τ_{180}. Differentiation of (11) with respect to ξ and switching the order of differentiation yields the fourteen differential equations

$$
\begin{aligned}
\dot{x}_-^\xi &= -\frac{\partial}{\partial \xi}(p_{-90} + p_{-+} + p_{90-})x_- - (p_{-90} + p_{-+} + p_{90-})x_-^\xi \\
&\quad + \frac{\partial}{\partial \xi}(p_{+-} - p_{90-})x_+ + (p_{+-} - p_{90-})x_+^\xi + \frac{\partial p_{90-}}{\partial \xi} \\
\dot{x}_+^\xi &= \frac{\partial}{\partial \xi}(p_{-+} - p_{90+})x_- + (p_{-+} - p_{90+})x_-^\xi \\
&\quad - \frac{\partial}{\partial \xi}(p_{+90} + p_{+-} + p_{90+})x_- - (p_{+90} + p_{+-} + p_{90+})x_-^\xi + \frac{\partial p_{90+}}{\partial \xi}
\end{aligned}
\tag{39}
$$

16

in the variables $x_+^\xi \equiv \frac{\partial x_+}{\partial \xi}, x_-^\xi \equiv \frac{\partial x_-}{\partial \xi}$. For an input field value $E(t_k)$, x_+ and x_- can be determined using the techniques detailed in Section 3.2.2, and the solution to (39) can be approximated using an implicit Euler discretization and Cramer's rule in a manner analogous to that detailed in Section 3.2.2.

To evaluate the derivatives of the likelihoods

$$p_{\alpha\beta} = \frac{1}{\tau_{\alpha\beta}} e^{-\gamma \Delta G_{\alpha\beta}^a} = \begin{cases} \frac{1}{\tau_{\alpha\beta}} e^{-\gamma \Delta G_0 (1 - F_{\alpha\beta}/F_c)^2} & , & F_{\alpha\beta} \leq F_c \\ 0 & , & F_{\alpha\beta} > F_c \end{cases}$$

we note that

$$\frac{\partial p_{\alpha\beta}}{\partial \gamma} = -\Delta G_{\alpha\beta}^a p_{\alpha\beta} \quad , \quad \frac{\partial p_{\alpha\beta}}{\partial \tau_{\alpha\beta}} = \frac{-1}{\tau_{\alpha\beta}} p_{\alpha\beta}$$

and

$$\frac{\partial p_{\alpha\beta}}{\partial \xi} = \begin{cases} \frac{2\gamma \Delta G_0}{F_c}(1 - F_{\alpha\beta}/F_c) p_{\alpha\beta} \frac{\partial F_{\alpha\beta}}{\partial \xi} & , & F_{\alpha\beta} \leq F_c \\ 0 & , & F_{\alpha\beta} > F_c. \end{cases}$$

The values of $\frac{\partial F_{\alpha\beta}}{\partial \xi}$ resulting from the relations (13) are compiled in Table 3.

ξ	$90+$	$+90$	$90-$	-90	$+-$	$-+$
P_R^+	E	$-E$	$-E$	E	$-2E$	$2E$
ε_R^+	σ	$-\sigma$	σ	$-\sigma$	0	0
ε_R^{90}	$-\sigma$	σ	$-\sigma$	σ	0	0
d_+	$E\sigma$	$-E\sigma$	$-E\sigma$	$E\sigma$	$-2E\sigma$	$2E\sigma$

Table 3: Values of the derivatives $\frac{\partial F_{\alpha\beta}}{\partial \xi}$.

4.2 Data-Driven Techniques for Initial Parameter Estimates

An ideal data set for obtaining data-driven initial parameter estimates and optimization-based final parameter values has two components: (i) saturated major loop and biased minor loop polarization and strain data, and (ii) creep polarization or strain data at two or more field values as depicted in Figure 4(a) and (b). If creep data is not available, frequency-dependent data, such as that depicted in Figure 4(c) can be used to provide an initial estimate for τ_{90}.
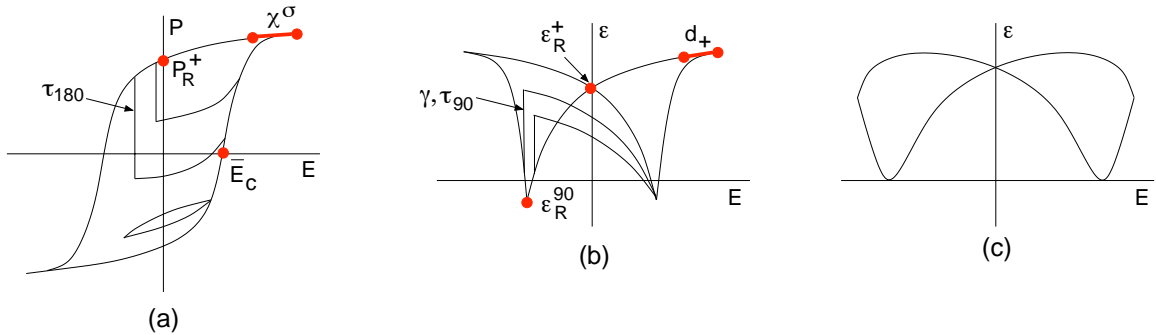

Figure 4: (a) and (b) Saturated major loop, minor loop, and creep data used to determine initial estimates for $P_R^+, \varepsilon_R^+, \varepsilon_R^{90}, \chi^\sigma, d_+, \gamma, \tau_{90}$ and τ_{180}. (c) Frequency-dependent strain data used to determine initial estimate for τ_{90} or τ_{180}.
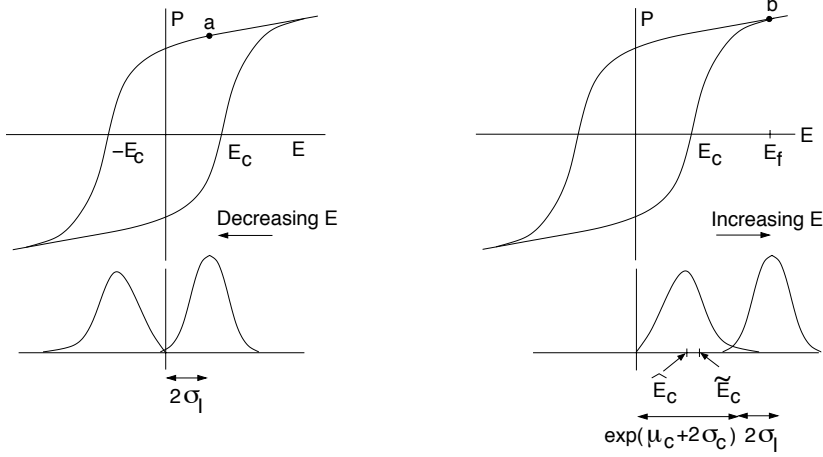
Figure 5: Polarization and field values used to obtain initial estimates for $\bar{F}_c, \sigma_c, \sigma_I$.

As noted in (7), the parameters to be estimated are $p = [P_R^+, \varepsilon_R^+, \varepsilon_R^{90}, \chi^\sigma, d_+, s^E, \gamma, \tau_{90}, \tau_{180}, \alpha_k, \beta_k]$. The representations (5) for the densities $\nu_c(F_c)$ and $\nu_I(E_I)$ additionally requires estimation of the coefficients $\bar{p} = [\bar{F}_c, \sigma_c, \sigma_I]$.

Data-driven techniques to estimate initial values for $P_R^+, \varepsilon_R^+, \varepsilon_R^{90}, \chi^\sigma, d_+, \bar{E}_c, \bar{F}_c, \sigma_c, \sigma_I$ are summarized in Table 4 with reference to Figures 4 and 5. The values of σ_I and σ_c are then used to construct the vectors $\vec{\sigma}_I = \{2^k \sigma_c\}$ and $\vec{\sigma}_c = \{2^k \sigma_c\}$ for the density basis functions $\phi_k(E_I)$ and $\varphi_k(F_c)$. One strategy to obtain initial values for the coefficients α_k and β_k is simply to take $\alpha_k = \beta_k = 1$. Documented values provide an initial estimate for s^E.

Initial Estimates for γ, τ_{90} and τ_{180} Based on Creep Data

Creep data collected at two or more fixed fields, as indicated by the thick lines in Figure 6, can be used to determine initial estimates for γ, τ_{90} and τ_{180}. Whereas either strain or polarization data can be employed, the former exhibits more sensitivity to 90° switching so we employ it here. The fixed field values are denoted by $\bar{E}_1$ and $\bar{E}_2$ as indicated by (1) and (2) for the strains plotted in Figure 6. We note that $\bar{E}_1$ designated by (1) satisfies $\bar{E}_1 < -E_c$. Finally, let t_0 designate the time at which the field was fixed, let $\varepsilon_1, \varepsilon_2$ and ε_3 designate measured strain values at equally spaced subsequent times $t_1 = t_0 + \Delta t, t_2 = t_0 + 2\Delta t$ and $t_3 = t_0 + 3\Delta t$, and let $e_2 = \varepsilon_2 - \varepsilon_1, e_3 = \varepsilon_3 - \varepsilon_2$.

Assumption 1. We assume that the decay behavior of dipole fractions can be adequately approximated by neglecting interaction fields and assuming that switches occur at $\pm E_c$. For a fixed field $E > E_c$, we assume that $x_- = 0$ and that $p_{90-} = p_{+90} = p_{+-} = 0$. Similarly, for $E < -E_c$, we assume that $x_+ = 0$ and that $p_{-90} = p_{90+} = p_{-+} = 0$.

With these simplifying assumptions, it follows from (2) that

$$\begin{aligned}
\dot{x}_- &= -p_{90-}x_- + p_{90-} \quad, \quad E < -E_c \\
\dot{x}_+ &= -p_{90+}x_+ + p_{90+} \quad, \quad E > E_c
\end{aligned} \tag{40}$$

For fixed fields, (40) has the analytic solution

$$\begin{aligned}
x_-(t, E) &= 1 - (x_-(t_0, E) - 1)e^{-(t-t_0)p_{90-}(E)} \quad, \quad E < -E_c \\
x_+(t, E) &= 1 - (x_+(t_0, E) - 1)e^{-(t-t_0)p_{90+}(E)} \quad, \quad E > E_c.
\end{aligned} \tag{41}$$

18

Parameter	Data or Source	Justification
P_R^+	Remanence polarization	
ε_R^+	Remanence strain	
ε_R^{90}	Minimum strain	
χ^σ	Slope of E-P curve prior to switching.	From the relation $P = \chi^\sigma E = \epsilon_0(\epsilon_r - 1)E$, it follows that the relative permittivity ϵ_r and χ^σ satisfy $\chi^\sigma = \epsilon_0(\epsilon_r - 1)$ where $\epsilon_0 = 8.85 \times 10^{-12}$ F/m is the permittivity of free space.
d_+	Slope of E-ε curve prior to switching.	Can be compared to documented material values.
s^E	Slope of σ-ε curve.	Can be compared to documented material values.
$\gamma, \tau_{90}, \tau_{180}$	Creep data as shown in Figure 4.	γ and τ_{90} given by solution of (43) using data from two fixed fields $\bar{E}_1$ and $\bar{E}_2$. We typically take $\tau_{180} = \frac{1}{10}\tau_{90}$.
$\alpha_k = \beta_k = 1$	*A priori* choice	
$\bar{E}_c$ $\bar{F}_c$ $\quad =$ $2P_R^+\bar{E}_c$	Coercive field E_c	Whereas the mode $\hat{E}_c$ most closely coincides with E_c (see Appendix B), by approximating with the median $\tilde{E}_c$, the relation $\tilde{E}_c = e^{\mu_c}$ from (50) can be used to obtain $\mu_c = \bar{E}_c$.
σ_I	a	Switching begins when $\nu_I(E_I)$ intersects $\nu_c(-E_c)$ with $2\sigma_I$ specifying the 94.5% confidence level.
σ_c	E_f: Polarization where switching completes for increasing E.	Occurs when $\nu_I(E_I)$ quits intersecting $\nu_c(E_c)$ at 94.5% confidence level. From (51), this yields $\sigma_c = \frac{1}{2}\ln((E_f - 2\sigma_I)/\tilde{E}_c)$ since $e^{\mu_c + 2\sigma_c} + 2\sigma_I = E_f$.

Table 4: Data-driven algorithms for initial parameter estimates with reference to Figures 4–6.

From Assumption 1, it follows that

$$\varepsilon(E, \sigma) \approx s^E \sigma + E \sum_{\alpha = \pm, 90} d_\alpha x_\alpha + \sum_{\alpha = \pm, 90} \varepsilon_R^\alpha x_\alpha$$

which, when combined with the physical assumptions in (4), yields

$$
\begin{aligned}
\frac{e_3}{e_2} &= \frac{[(Ed_+ + \varepsilon_R^+ - \varepsilon_R^{90})x_+(t_3, E) + \varepsilon_R^{90}] - [(Ed_+ + \varepsilon_R^+ - \varepsilon_R^{90})x_+(t_2, E) + \varepsilon_R^{90}]}{[(Ed_+ + \varepsilon_R^+ - \varepsilon_R^{90})x_+(t_2, E) + \varepsilon_R^{90}] - [(Ed_+ + \varepsilon_R^+ - \varepsilon_R^{90})x_+(t_1, E) + \varepsilon_R^{90}]} \\
&= \frac{x_+(t_3, E) - x_+(t_2, E)}{x_+(t_2, E) - x_+(t_1, E)}
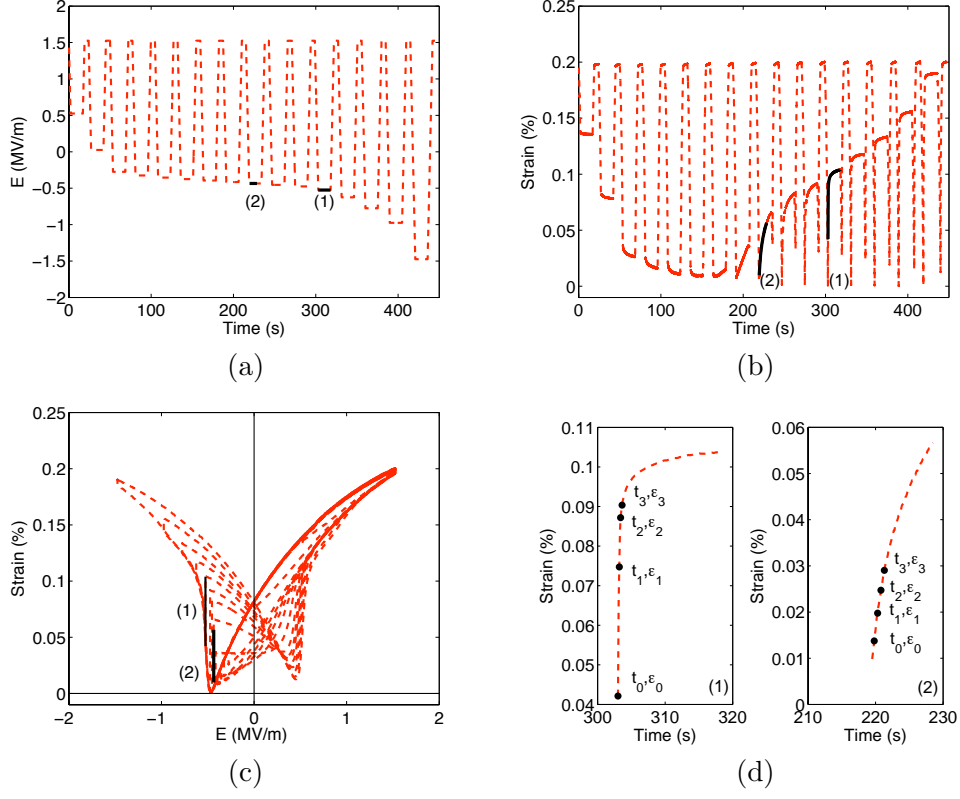\end{aligned}
\tag{42}
$$

19

Figure 6: Zero prestress strain data from [24] used to obtain initial estimates of γ and τ_{90}.

for $E > E_c$. The expression for $E < -E_c$ is identical. From (3), (41) and (42), it follows that

$$
\begin{aligned}
\frac{1}{\tau_{90}} e^{-\gamma \Delta G^a_{90-}(E)} &= \frac{1}{\Delta t} \ln \left(\frac{e_2}{e_3} \right) \quad , \quad E < -E_c \\
\frac{1}{\tau_{90}} e^{-\gamma \Delta G^a_{90+}(E)} &= \frac{1}{\Delta t} \ln \left(\frac{e_2}{e_3} \right) \quad , \quad E > E_c.
\end{aligned}
\tag{43}
$$

We note that if $|E| > E_c$, as is the case for the data at $\bar{E}_1$ indicated in Figure 6 by (1), energy barriers are eliminated so that $\Delta G^a_{-90}(E) = \Delta G^a_{+90}(E) = 0$ which yields

$$
\tau_{90} = \frac{\Delta t}{\ln(e_2/e_3)}.
$$

In this case, the decay data at the second fixed field can be used to solve for γ. If $|E| < E_c$ for both fixed fields, or if E_c is unknown, one can eliminate τ_{90} to first solve for γ. To illustrate for $\bar{E}_1, \bar{E}_2 < 0$ and corresponding strain differences e_{12}, e_{13} and e_{22}, e_{23}, elimination of τ_{90} yields the relation

$$
e^{\gamma \Delta G^a_{-90}(\bar{E}_1)} \ln(e_{12}/e_{13}) = e^{\gamma \Delta G^a_{-90}(\bar{E}_2)} \ln(e_{22}/e_{23})
\tag{44}
$$

for γ. Note that (44) can be easily solved for γ by plotting the solution as a function of γ_2 and approximating the root or by using a symbolic routine; e.g., the symbolic MATLAB command `solve.m`. The parameter τ_{90} is then determined from (43). An initial value of τ_{180} is then taken to be $\tau_{180} = \frac{1}{10} \tau_{90}$.

20

The data-driven algorithm to determine initial parameter estimates for the 180^0 switching polarization model (16) is analogous.

Initial Estimates for τ_{90} Based on Frequency-Dependent Data

Frequency-dependent strain or polarization data, such as that plotted in Figures 4 and 7, can be used in a similar manner to obtain an initial estimate for τ_{90} or τ_{180}. We let t_0 denote the time at which a field reversal occurs at $E_{\max}$ or $E_{\min}$. As before, we let $\varepsilon_1, \varepsilon_2$ and ε_3 designate measured strains at equally spaced subsequent times $t_1 = t_0 + \Delta t, t_2 = t_0 + 2\Delta t$ and $t_3 = t_0 + 3\Delta t$, and let $e_2 = \varepsilon_2 - \varepsilon_1, e_3 = \varepsilon_3 - \varepsilon_2$.

Assumption 2. For a field reversal at $E_{\max}$, we make the simplifying assumption that $x_- \approx 0$ and that dipole kinetics are dominated by switching from 90° to 180° orientations; i.e., $p_{90-} = p_{+90} = p_{+-} = 0$. Similarly, for reversal at $E_{\min}$, we assume that $x_+ \approx 0$ and $p_{-90} = p_{90+} = p_{-+} = 0$. These are the same assumptions made in Assumption 1. Finally, we assume that activation energies are sufficiently small to permit the approximation

$$p_{90+} = p_{90-} = \frac{1}{\tau_{90}}. \tag{45}$$

With these assumptions, (11) reduces to

$$\dot{x}_- = \frac{-1}{\tau_{90}}x_- + \frac{1}{\tau_{90}} \quad , \quad E \approx E_{\min}$$
$$\dot{x}_+ = \frac{-1}{\tau_{90}}x_+ + \frac{1}{\tau_{90}} \quad , \quad E \approx E_{\max} \tag{46}$$

which has the solution

$$x_-(t, E) = 1 - (x_-(t_0, E) - 1)e^{-(t-t_0)/\tau_{90}} \quad , \quad E \approx E_{\min}$$
$$x_+(t, E) = 1 - (x_+(t_0, E) - 1)e^{-(t-t_0)/\tau_{90}} \quad , \quad E \approx E_{\max}. \tag{47}$$

If we assume that $E_1 d_+ \approx E_2 d_+ \approx E_3 d_+ \approx E_{\max}$, analysis similar to that used to obtain (42) yields the relation

$$\tau_{90} = \frac{\Delta t}{\ln(e_2/e_3)} \tag{48}$$

which provides an initial, data-driven estimate for τ_{90}. Due to the assumption (45), which is more stringent than the case for creep data where fields are fixed, this data does not readily admit a data-driven algorithm to initially estimate γ. Hence it must simply be estimated through a least squares fit to data.
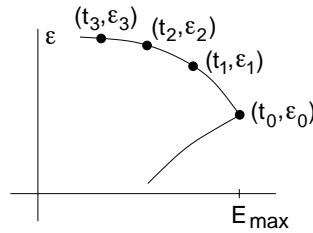

Figure 7: Frequency-dependent strain data used to obtain an initial estimate for τ_{90}.

5   Model Calibration and Validation for PZT and BaTiO₃

We illustrate the performance of the data-driven parameter estimation algorithms using PZT data reported in [24] and BaTiO₃ data from [5].

For the PZT data, polarization and strain measurements, in the absence of applied mechanical stresses, were collected using a P-802.00 piezo-actuator whereas a prestressed NEC Model AEO505D08 actuator with a restoring spring was used to collect stress-dependent data. Both are multilayer devices with similar dimensions so we briefly summarize the latter and refer the reader to [24] for details regarding both devices.

The AEO505D08 actuator was comprised of 80 active layers, each of thickness 0.1 mm. The dimensions, including packaging, were $6.5 \times 6.5 \times 10$ mm which yielded the cross-sectional area $A = 42.25$ mm$^2 = 4.225 \times 10^{-5}$ m^2. The polarization was measured using a Sawyer-Tower circuit comprised of a reference capacitor connected in series with the PZT actuator. Displacements were measured using a fiber-optic displacement sensor having an effective resolution of 0.1 μm and strains were computed by dividing the total thickness (8 mm) of the active layers.

When reporting the accuracy of model fits, we define the relative errors to be

$$e_{rel} = \frac{\sum_{i=1}^{N_d} \left(w_P[P(E(t_i), \sigma; q) - P_i]^2 + w_\varepsilon[\varepsilon(E(t_i), \sigma; q) - \varepsilon_i]^2 \right)}{\sum_{i=1}^{N_d} \left(w_P P_i^2 + w_\varepsilon \varepsilon_i^2 \right)}.$$

The functionals (34) and (35), with the analytic Jacobians constructed using the algorithms in Section 4.1, were minimized using the MATLAB nonlinear least squares routine `lsqnonlin` with the options 'Algorithm'='trust-region-reflective', 'TolFun'=$1e-4$, 'Jacobian'='on' and a lower bound of 0 specified for all parameters except ε_R^{90} which was bounded below by -1×10^{-2}.

5.1   Zero Prestress PZT Data

90° Polarization-Strain Model

We first illustrate the calibration and performance of the 90° switching polarization-strain model (8) and 180° switching polarization model (16) using zero prestress data reported in [24] obtained using a P-802.00 PZT actuator.

The data used to obtain initial parameter values is plotted in Figures 6 and 8 and resulting values, obtained using the algorithms in Table 4 are compiled in Table 5. Corresponding model predictions and initial density representations are respectively plotted in Figure 9 and Figure 11(a) and (c). The
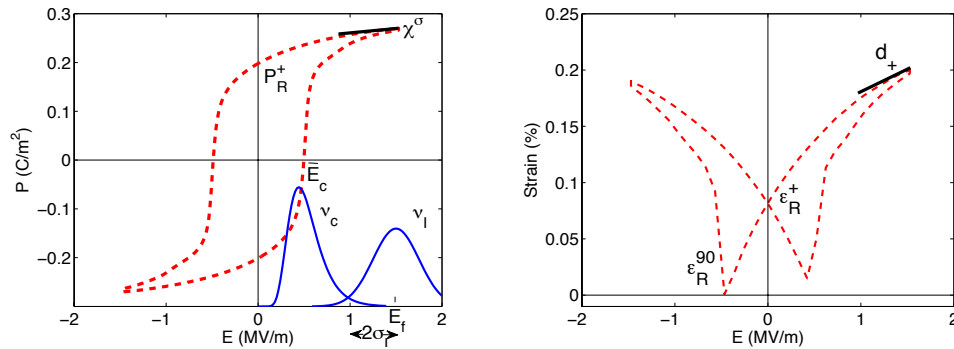

Figure 8: Zero prestress polarization and strain data from [24] used to obtain initial estimates of $P_R^+, \varepsilon_R^+, \varepsilon_R^{90}, \chi^\sigma, \bar{F}_c, \sigma_c$ and σ_I.
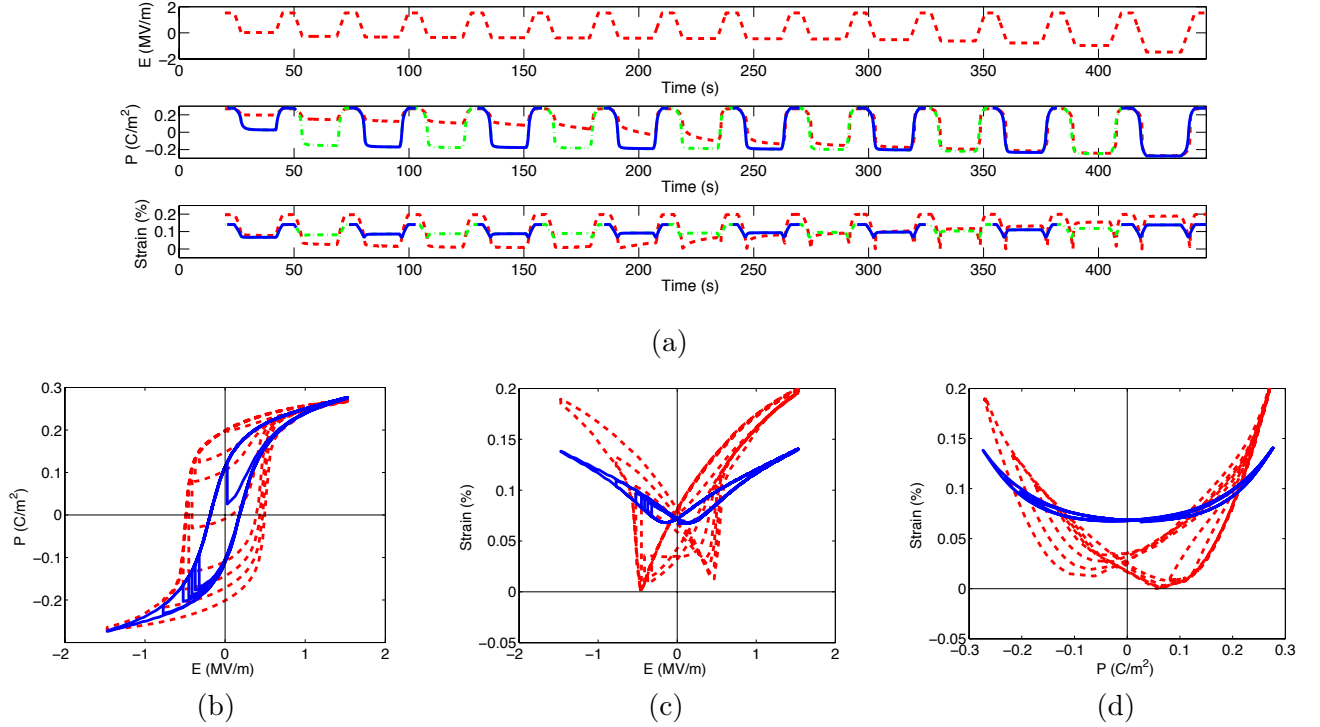
Figure 9: Polarization and strain model prediction to zero-prestress data from [24] using initial parameter values obtained using the data-driven algorithms in Table 4: (a) time domain and (b)-(d) phase space; (- - -) experimental data, (- • - •) model fit, (———) model fits for 8 selected loading cycles. Labels (1) and (2) in Figure 6 indicate strain data used to find initial estimates for γ and τ_{90}.

initial values of $P_R^+, \varepsilon_R^+, \varepsilon_R^{90}$ and χ^σ are obtained directly from the polarization and stain data shown in Figure 8. The density coefficient $\bar{F}_c = P_R^+ \bar{E}_c$ results from $\bar{E}_c = 0.5 \times 10^6$, and $2\sigma_I = 0.5 \times 10^6$ yields $\sigma_I = 0.25 \times 10^6$. Similarly, the relations in Figure 5 yield $\sigma_c = 0.5 \log((1.5 - 0.5)/0.5) \approx 0.35$. Finally, the initial estimates for γ and τ_{90} were computed using the data shown in Figure 6. The initial value $d_+ = 374 \times 10^{-12}$ is a literature value of d_{33} reported for PZT.

Whereas the model quantifies the trends exhibited by the data, the initial predictions are not sufficiently accurate for material or device characterization. We then minimized the functional (35) using 2140 data values to obtain the optimized parameters reported in Table 5 and the resulting fits and densities shown in Figure 10 and 11(b) and (d). The optimized relative error is 10.99% It is observed that the calibrated polarization and strain models accurately fit the data in all drive regimes including the saturation and burst regions, the creep regions, and minor loops. Moreover, use of the analytic Jacobian and efficient implementation algorithms permitted the optimization to

	P_R^+	ε_R^+	ε_R^{90}	χ_+^σ	d_+	γ	τ_{90}	τ_{180}
Init.	0.2	0.081×10^{-2}	0.0	4.71×10^{-8}	374×10^{-12}	1.38×10^{-4}	0.64	.064
Opt.	0.18	0.050×10^{-2}	-5.64×10^{-2}	5.35×10^{-8}	930.46×10^{-12}	2.08×10^{-3}	0.41	.043

Table 5: Initial and optimized parameter values for the polarization and strain model with zero prestress. The fixed density parameters were $\bar{F}_c = 0.2 \times 10^6, \sigma_I = 0.25 \times 10^6$ and $\sigma_c = 0.35$. The optimized density parameters $\alpha_1 = 1.65, \alpha_0 = 0.92, \alpha_{-1} = 0.77, \alpha_{-2} = 2.55, \alpha_{-3} = 6.69$ and $\beta_1 = 0.79, \beta_0 = 1.24, \beta_{-1} = 1.12, \beta_{-2} = 2.95, \beta_{-3} = 9.45$ were obtained using initial estimates of 1.
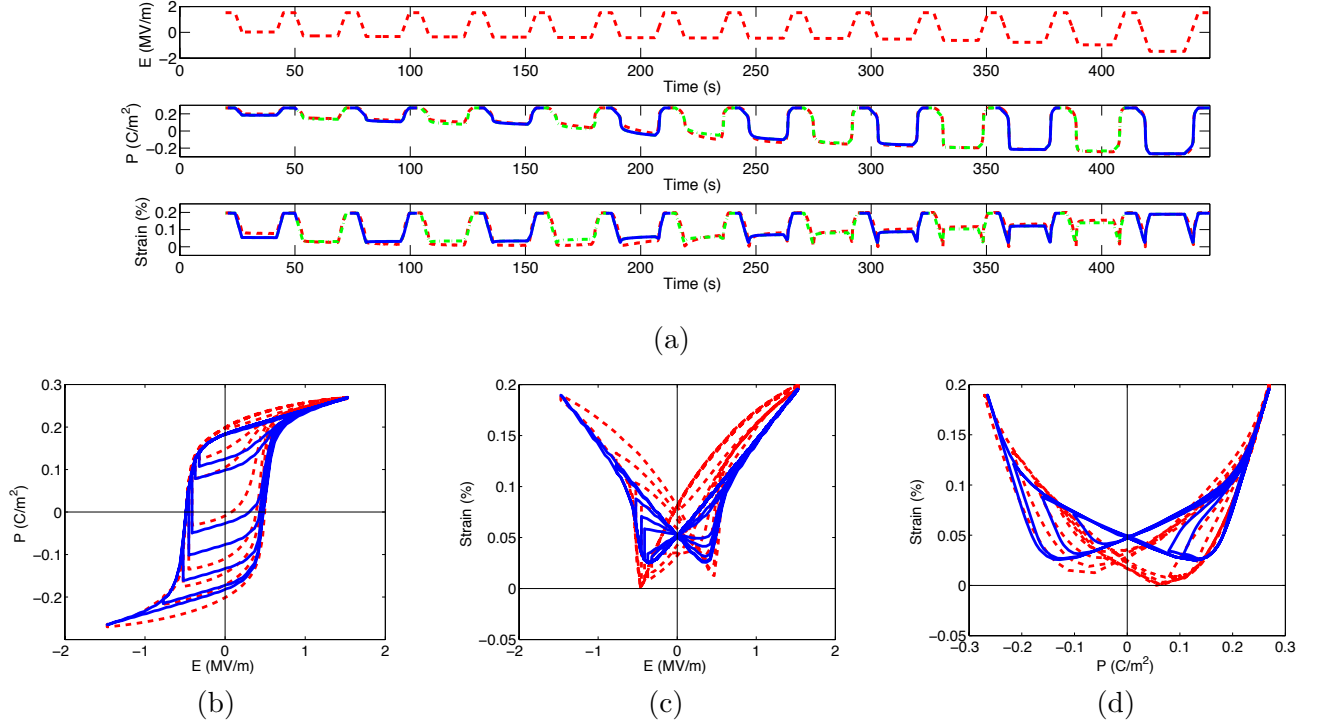
23

Figure 10: Optimized fit of the polarization and strain model to zero-prestress data from [24]: (a) time domain and (b)-(d) phase space; (– – –) experimental data, (– • – •) model fit, (———) model fits for 8 selected loading cycles.

be completed in 673 s on a Mac Pro with a 2.26 GHz processor and 8 GB of memory.

We note that the final parameter values in Table 5 are quite close to the initial values predicted by the data-driven algorithms. Hence much of the inaccuracy in the initial model prediction is due to the initial density parameter choices $\alpha_k = \beta_k = 1$. The initial values of α_k and β_k can be easily tuned to provide more accurate fits; however, the choice of 1 simplifies the data-driven algorithms and is sufficiently accurate so that the optimization routine yields accurate fits in a timely manner.
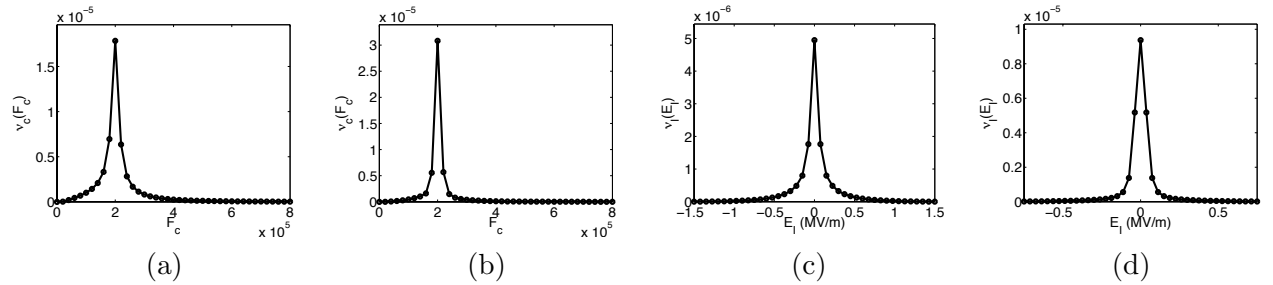

Figure 11: (a) Initial and (b) optimized critical driving force density $\nu_c(F_c)$ with 41 equally spaced quadrature points marked as dots. (c) Initial and (d) optimized interaction field density $\nu_I(E_I)$.

180° Polarization Model

For applications and operating regimes with negligible to moderate prestresses σ_0, the field-polarization response exhibits minimal dependency on 90° switching. In these cases, the polarization can be adequately modeled using the 180° switching model summarized in Table 2.

	P_R	η^σ	γ	τ_{90}
Init.	0.2	0.25×10^8	2.79×10^{-3}	0.15
Opt.	0.20	0.22×10^8	3.78×10^{-3}	0.10

Table 6: Initial and optimized parameter values for the 180° model zero prestress.

To illustrate, we employed the data-driven algorithms of Section 4.2 to obtain the parameter estimates compiled in Table 6. We then minimized the functional (34) using 2140 data points to obtain the optimized fit and densities shown in Figure 12. The accuracy of the fit demonstrates the applicability of the 180° switching model for characterizing the polarization in low to moderate stress regimes. Moreover, the use of the implementation algorithms of Section 3 and analytic Jacobian relations of Section 4.1 renders the model calibration codes highly efficient and optimization was achieved in approximately 36 s on the Mac Pro.
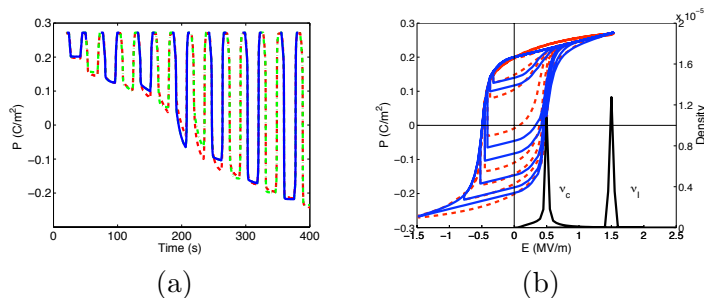

Figure 12: Optimized fit of the 180° polarization model to zero-prestress data from [24]: (a) time domain and (b) phase space; (– – –) experimental data, (– • – •) model fit, (———) model fits for 8 selected loading cycles.

5.2 Prestressed Actuator

The estimation of parameters and performance of the polarization-strain model for a prestressed actuator is illustrated in [19] using data reported in [24].

5.3 Variable Loading Rates

To illustrate the physical phenomena, and resulting model response, associated with variable loading rates, we consider data from [24] that was collected at loading rates of 5 V/s, 50 V/s and 500 V/s. Since this data was collected using the P-802.00 actuator, that had purely electrical loading, the polarization and strains were modeled using the relations (8) that neglect the prestress σ_0 and spring and damping coefficients k and c associated with restoring mechanisms.

The strain and polarization data plotted in Figure 13 exhibit differing dynamics at the three loading rates, especially in the burst region where $+180^o$ to 90° and 90° to -180° dipole transitions are dominant. In the field-polarization plots, this is reflected by delayed first-order minor loops as indicated by the curves (1)-(3). The slower 90° to -180° transitions, and resulting lagging effects at high loading rates, are even more noticeable in the field-strain plots due to the degree to which stains depend on 90° dipole switching.

To model this rate-dependent phenomena, the data-driven techniques were used to compute the initial parameter estimates compiled in Table 7 along with the density coefficients $\bar{F}_c = 0.2\times10^6, \sigma_c = 0.347$ and $\sigma_I = 0.25 \times 10^6$. We then minimized the functional (43), using the 5 V/s and 500 V/s
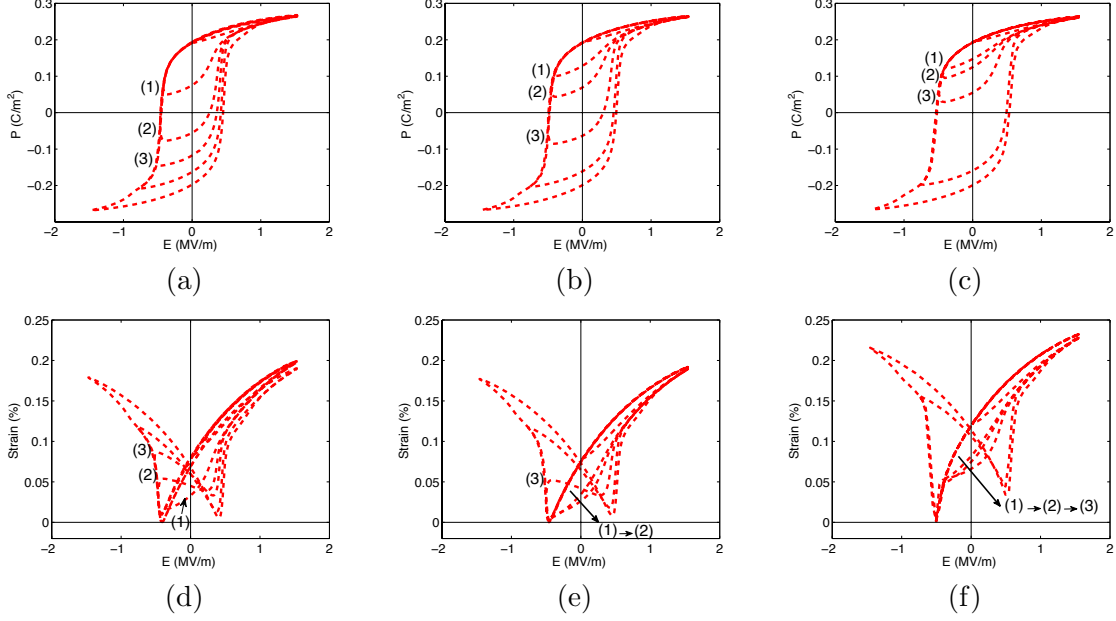
Figure 13: Polarization and strain data from [24], collected at (a),(d) 5 V/s, (b),(e) 50 V/s, and (c),(f) 500 V/s.

data, with $w_P = 1, w_\varepsilon = 40,000$, to obtain the optimized parameters in Table 7, the densities shown in Figure 14, and the model fits plotted in Figure 12. We note that the model is predicting the 50 V/s behavior.

The time-polarization and time-strain plots illustrate that the model is quantifying both the major and minor loop behavior at the three loading rates. The phase plots illustrate that while the model is very accurately characterizing the field-polarization behavior, there is some inaccuracy in the field-strain fits and prediction. This may be due to limitations in the relations used to quantify 90° and 180° switching mechanisms. However, the model is quantifying the lagged switching behavior at 500 V/s that is present in both the polarization and strain data. We note that improved fits for each loading rate can be achieved if parameters are optimized for that rate. The dynamic nature of the model is illustrated by the fact that it adequately characterizes the rate-dependent material behavior using one set of parameters. This makes it advantageous for material characterization, device optimization, and control design of applications requiring variable loading rates.
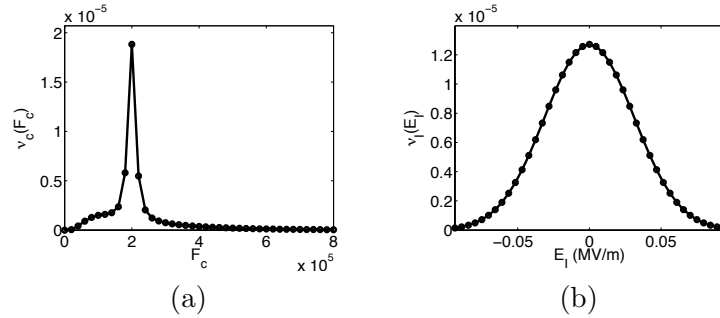

Figure 14: (a) Critical driving force density $\nu_c(F_c)$ and (b) interaction field density $\nu_I(E_I)$ with 41 equally spaced quadrature points marked as dots.
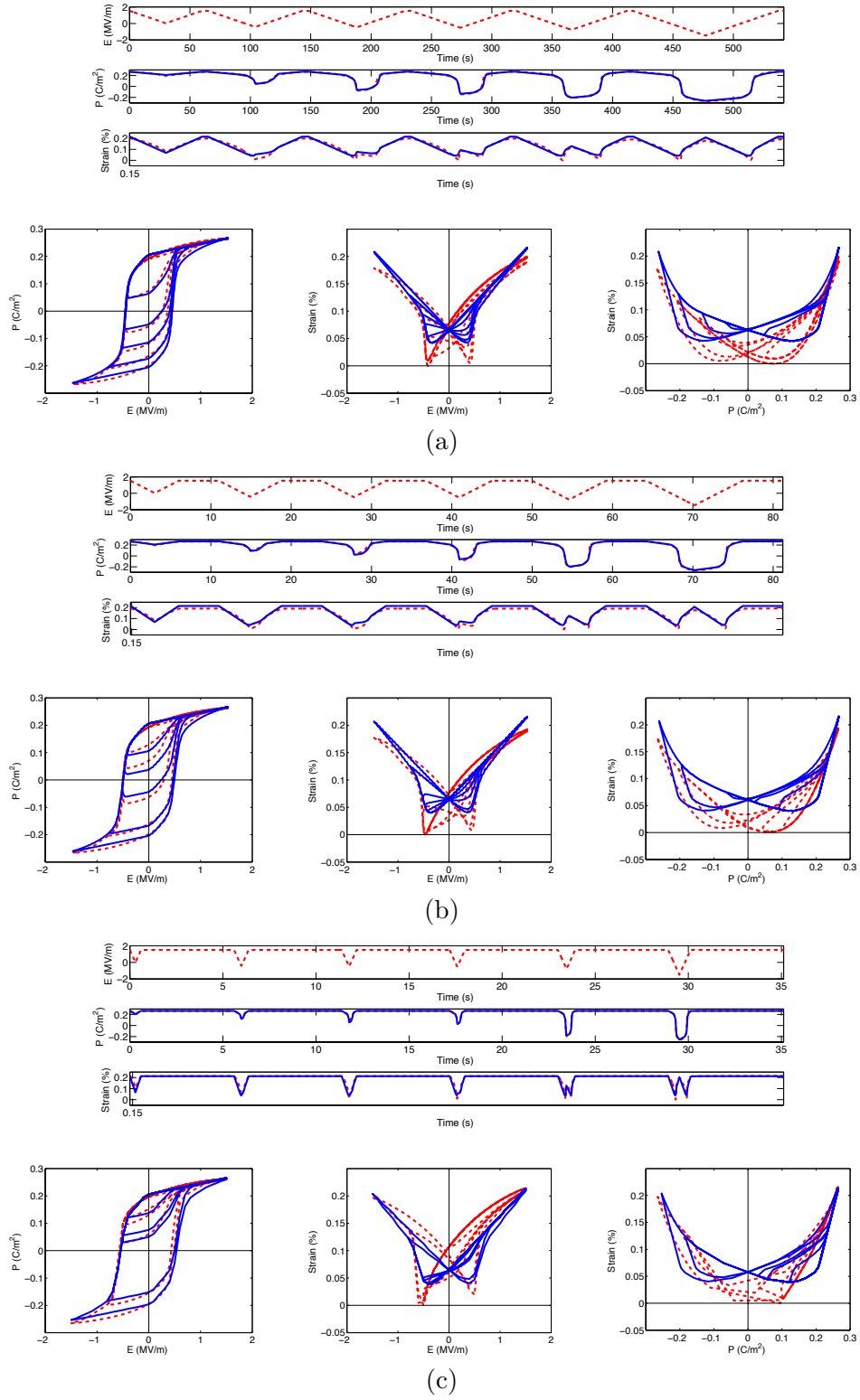
26

Figure 15: Optimized fit of the polarization-strain model to data from [24] for loading rates of (a) 5 V/s and (c) 500 V/s. (b) Model prediction for a loading rate of 50 V/s: (‐ ‐ ‐) experimental data, (———) model fit.

27

	P_R^+	ε_R^+	ε_R^{90}	χ_+^σ	d_+	γ	τ_{90}	τ_{180}
Init	0.18	0.050×10^{-2}	-5.64×10^{-2}	5.35×10^{-8}	930.46×10^{-12}	2.08×10^{-3}	0.41	0.043
Opt	0.21	0.066×10^{-2}	-0.071×10^{-2}	3.93×10^{-8}	992.26×10^{-12}	8.37×10^{-3}	1.48×10^{-9}	0.16

Table 7: Initial and optimized parameter values for the polarization and strain model obtained using loading rates of 5 V/s and 500 V/s. The optimized density parameters are $\alpha_1 = 5.02, \alpha_0 = 1.82 \times 10^{-2}, \alpha_{-1} = 1.24, \alpha_{-2} = 2.56, \alpha_{-3} = 2.89$ and $\beta_1 = 4.63 \times 10^{-2}, \beta_0 = 1.13 \times 10^{-8}, \beta_{-1} = 4.71 \times 10^{-8}, \beta_{-2} = 3.42 \times 10^{-14}, \beta_{-3} = 11.01$.

5.4 Single Crystal BaTiO$_3$

Here we illustrate the performance of the model for characterizing the behavior of single crystal BaTiO$_3$ using data from [5]. For the data considered here, the applied stress was parallel to the applied field thus motivating consideration of a uniaxial model. Furthermore, we employ the grain-level or single crystal relations (10).

We first determined the initial and optimized parameter values reported in Table 8 through a fit to the data collected at prestresses of -0.36 MPa and -1.78 MPa. The correlation of the parameter values for $P_R^+, \varepsilon_R^+, \varepsilon_R^{90}, \chi_+^\sigma$ and d_+ to corresponding properties of the data can be directly observed. We also note that $\tau_{90} > \tau_{180}$ which indicates that 180° switching occurs more quickly than 90° switching. This is consistent with analogous observations for PZT, reported in [23], and explains the flat behavior of the P-ε data.

The resulting fit at -0.36 MPa and -1.78 MPa and predictions at prestresses of -0.72 MPa and 0 MPa are shown in Figure 16. It is observed that the polarization and strain fits at -0.36 MPa and -1.78 MPa are quite accurate as are the polarization predictions at the other two prestresses. Whereas the strain prediction at -0.72 MPa is moderately accurate, the model overpredicts the strains for the unstressed crystal where 90° switching is minimal. This is in accordance with the results reported in [12] and indicates some limitations in the 90° switching characterization in the absence of prestresses.

	P_R^+	ε_R^+	ε_R^{90}	χ_+^σ	d_+	s^E	γ	τ_{90}	τ_{180}
Init	0.26	0.67×10^{-2}	-0.12×10^{-2}	1.5×10^{-8}	85.6×10^{-12}	15.7×10^{-12}	0.015	0.06	0.01
Opt	0.25	0.73×10^{-2}	-0.99×10^{-2}	2.82×10^{-8}	841.89×10^{-12}	26.83×10^{-11}	0.00041	0.34	0.00041

Table 8: Initial and optimized BaTiO$_3$ parameter values obtained through a fit to -0.36 MPa and -1.78 MPa prestressed data from [5]. The density representation (14) employed the optimized value $\bar{F}_c = 0.0145 \times 10^6$.

6 Concluding Remarks

The homogenized energy model is a multiscale, micromechanical framework that quantifies hysteresis and constitutive nonlinearities intrinsic to ferroelectric materials. It incorporates mechanisms at multiple spatial scales by combining energy analysis at the domain level with stochastic homogenization techniques to construct material-level constitutive relations. The multiple timescales associated with dipole switching processes are incorporated by employing Boltzmann principles to quantify transition rates associated with dipole fractions. In combination, the framework characterizes a range of rate-dependent hysteretic phenomena associated with the materials. Furthermore, constitutive
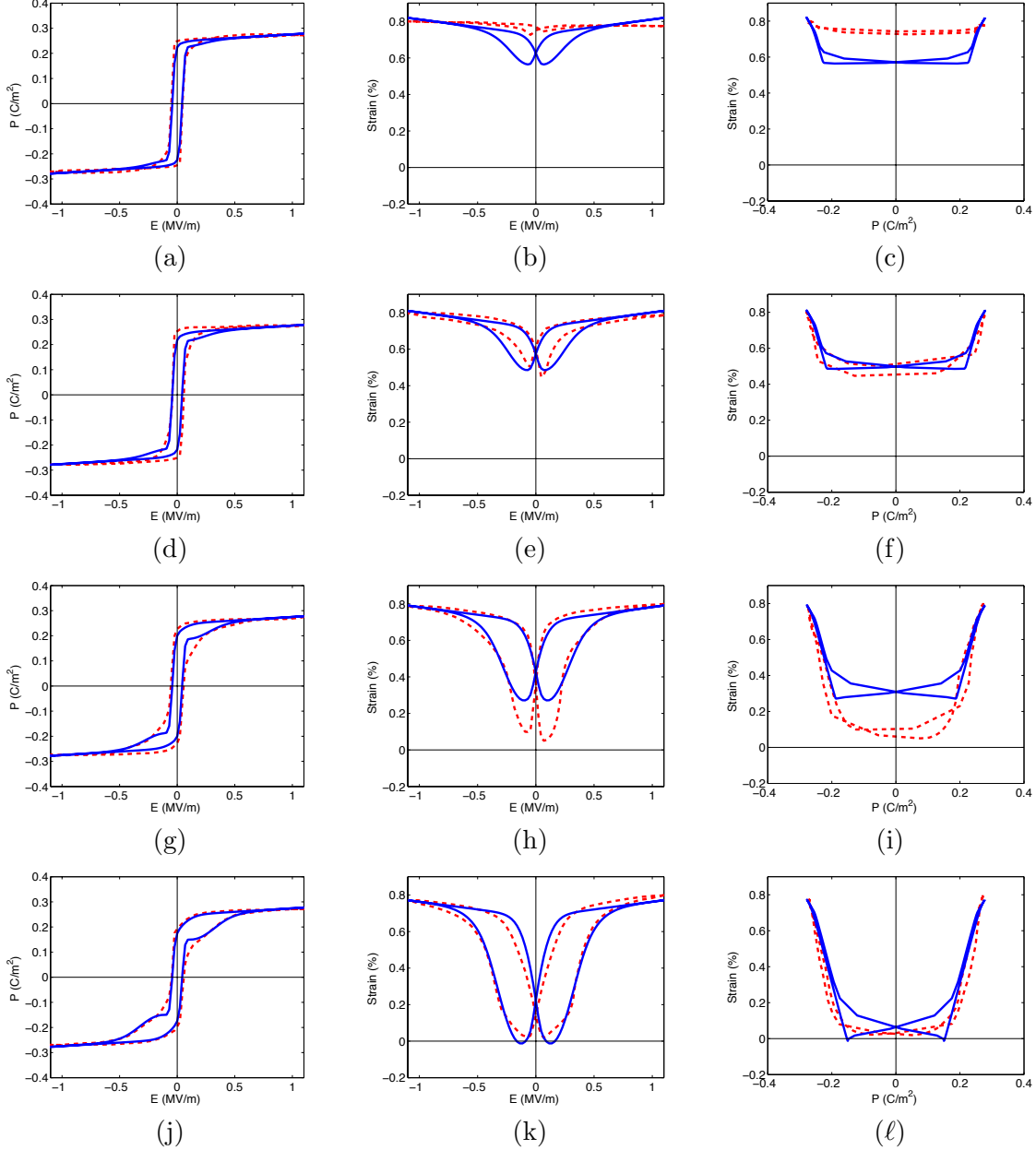
Figure 16: Fit of the polarization and strain model to single crystal BaTiO$_3$ data from [5] with a prestress of (d)-(f) -0.36 MPa and (j)-(ℓ) -1.78 MPa. Model predictions for prestresses of (a)-(c) 0 MPa and (g)-(i) -1.07 Mpa: (– – –) experimental data, (———) model fit.

relations resulting from the framework can be directly employed to construct distributed models, for complex devices, that are amenable to finite element implementation.

In this paper, we presented algorithms that facilitate efficient model calibration and implementation. The efficiency of the parameter estimation algorithms is based in part on the physical nature of the model which permits model parameters to be correlated with properties of field-polarization and field-strain data as shown in Figure 4. Specifically, we presented data-driven algorithms to determine initial estimates for $P_R^+, \varepsilon_R^+, \varepsilon_R^{90}, \chi^\sigma, d_+, \gamma, \tau_{90}, \tau_{180}$ that facilitate subsequent optimization through least squares fits to the data. Furthermore, this data can be used to determine values for

29

the density coefficients, $\bar{E}_c, \bar{F}_c, \sigma_c$ and σ_I.

Major loop, biased minor loop, and creep data, of the form depicted in Figure 4, represents ideal data to be collected if there is flexibility regarding the design of characterization experiments. However, in many cases, one is limited to biased minor loop data such as that shown in Figure 1. In such cases, one can employ values previously reported in the literature as initial values for optimization routines.

The coefficients d_{33} and s^E and relative permittivity ϵ_r, which can be used to compute χ_σ, are commonly reported for ferroelectric materials and documented values can be employed as initial parameter estimates. The remanence polarization P_R, remanence strain ε_R, and coercive field E_c are also fundamental properties of ferroelectric materials that are often reported only in material characterization investigations rather than in compilations for transducer design. The model parameters $P_R^+, \varepsilon_R^+, \varepsilon_R^{90}, \gamma, \tau_{90}$ and τ_{180} are related to intrinsic material properties that are critical to actuator and sensor design and characterization.

This motivates the compilation of material property and parameter tables and libraries that facilitate the calibration of models for devices that employ these materials. Representative values of $d_{33}, s_{11}^E, \epsilon_r, \chi^\sigma$ from the literature and P_R, ε_R, E_c from the data employed here, and in the companion paper [19], are respectively compiled in Tables 9 and 10. Similarly, representative values of $P_R^+, \varepsilon_R^+, \varepsilon_R^{90}, \gamma, \tau_{90}, \tau_{180}$ for PZT, PLZT and BaTiO$_3$ are summarized in Table 11. We note that while variations in these parameters exist for differing devices and operating regimes, these representative values can be employed to initialize optimization routines. Furthermore, it is noted in Appendix A that we are developing a website of data libraries, simulation codes, and modeling frameworks for ferroelectric, ferromagnetic, and ferroelastic materials. Data properties and parameters that can be used for material and device characterization will be compiled and updated at this site.

	d_{33} (pC/N)	s_{11}^E (m^2/N)	ϵ_r (C/Vm)	$\chi^\sigma = \epsilon_0(\epsilon_r - 1)$ (C/Vm)
PZT-5A	374	1.88×10^{-11}	1800	1.59×10^{-8}
BaTiO$_3$	85.6	8.05×10^{-12}	163	1.47×10^{-9}
PLZT	1188	1.47×10^{-11}	6356	2.99×10^{-8}

Table 9: Material properties for PZT-5A [17], BaTiO$_3$ [10] and PLZT [14]. Note that the free space permittivity has the value $\epsilon_0 = 8.85 \times 10^{-12}$.

	P_R (C/m^2)	ε_R (Unitless)	E_c (MV/m)
PZT-5A	0.2	0.081×10^{-2}	0.5
BaTiO$_3$	0.26	0.67×10^{-2}	0.05
PLZT	0.25	0.25×10^{-2}	0.36

Table 10: Remanence polarizations, remanence strains, and coercive fields for the PZT data [24], single crystal BaTiO$_3$ data [5] and PLZT data [14].

A   Available Codes

To facilitate model validation and dissemination to the community, we have made codes and data available at the website `http://www4.ncsu.edu/~jhcrews/smart/code/pzt/index.html`.

	P_R^+	ε_R^+	ε_R^{90}	χ_+^σ	d_+	γ	τ_{90}	τ_{180}
PZT	0.18	0.050×10^{-2}	-5.64×10^{-2}	5.35×10^{-8}	930.46×10^{-12}	2.08×10^{-3}	0.41	0.043
BaTiO$_3$	0.25	0.73×10^{-2}	-0.99×10^{-2}	2.82×10^{-8}	841.89×10^{-12}	4.1×10^{-4}	0.34	0.00041
PLZT	0.24	0.13×10^{-2}	-0.03×10^{-2}	10.06×10^{-8}	1390.5×10^{-12}	9.62×10^{-4}	0.032	0.70

Table 11: Representative parameter values for PZT, BaTiO$_3$ and PLZT. Appropriate units are given in the notation table in Section 1.

B   Lognormal Density

We summarize here aspects regarding the lognormal density that are pertinent to constructing coercive field densities. Details can be found in [1, 11].

If $Y \sim N(\mu, \sigma)$ is a normal random variable with mean μ and standard deviation σ, $X = \exp(Y)$ is lognormally distributed, $X \sim \ln N(\mu, \sigma)$, with density

$$f(x; \mu, \sigma) = \frac{1}{x\sigma\sqrt{2\pi}} e^{-(\ln x - \mu)^2 / 2\sigma^2}. \tag{49}$$

The mean $\bar{x}$, mode $\hat{x}$, median $\tilde{x}$ and variance $\bar{\sigma}^2$ of X are related to μ and σ by way of the relations

$$\bar{x} = E[X] = e^{\mu + \sigma^2/2} \quad , \quad \hat{x} = e^{\mu - \sigma^2}$$
$$\tilde{x} = e^{\mu} \qquad\qquad\qquad , \quad \bar{\sigma}^2 = \mathrm{var}[X] = \left(e^{\sigma^2} - 1\right) e^{2\mu + \sigma^2}. \tag{50}$$

As illustrated in Figure 17, the mean, mode and median differ due to the skewed nature of the density. We note that for the normal density, μ and σ have the same units as x whereas the physical meaning of these units is lost in the lognormal relations (50).

The dependence of f on μ and σ is illustrated in Figure 18. Note that X approaches a normal density with $\bar{x} = \tilde{x} = \hat{x} = e^{\mu}$ as σ decreases and the density limits to the Dirac density at e^{μ} as $\sigma \to 0$.

As noted on page 9 of [1], the qth quantile of the lognormal density can be expressed as

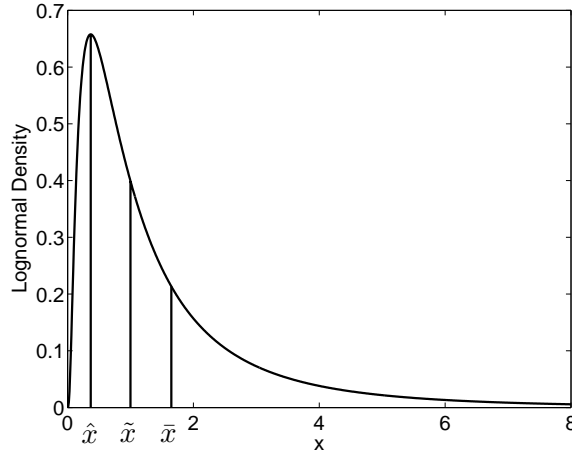$$\left[e^{\mu - q\sigma}, e^{\mu - q\sigma}\right] \tag{51}$$

Figure 17: Mode $\hat{x}$, median $\tilde{x}$ and mean $\bar{x}$ of the lognormal density with $\mu = 0, \sigma = 1$.

as illustrated in Figure 19. This relation, along with (50), will be used in Section 4.1 to specify initial density parameter values in terms of measured properties of polarization and magnetization data. For example, two standard deviations, which represents a probability of 94.5% is plotted for normal and lognormal densities in Figure 19.
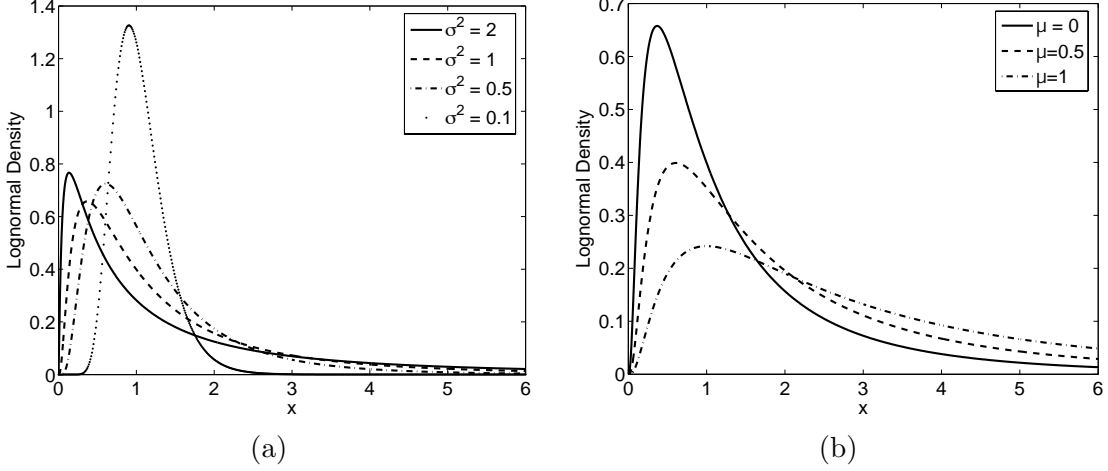

(a)   (b)

Figure 18: Dependence of the lognormal density on (a) σ^2 with $\mu = 0$, and (b) μ with $\sigma^2 = 1$.

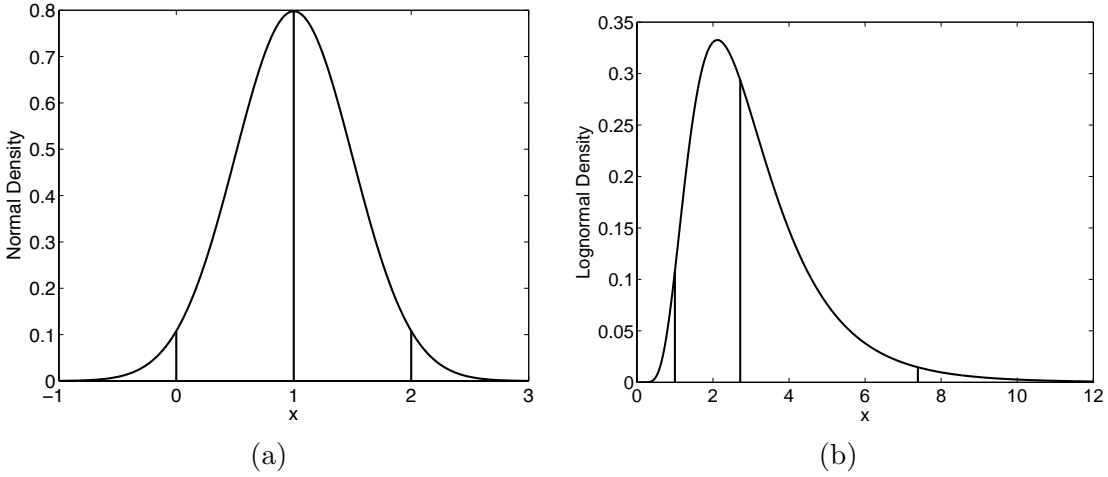(a)   (b)

Figure 19: Median values and 94.5% confidence intervals with $\mu = 1$, $\sigma = 0.5$ for a (a) normal density $[\mu - 2\sigma, \mu + 2\sigma]$, and (b) lognormal density $\left[e^{\mu - 2\sigma}, e^{\mu + 2\sigma}\right]$.

Acknowledgements

References

[1] J. Aitchison and J.A.C. Brown, *The Lognormal Distribution*, Cambridge University Press, Cambridge, UK, 1963.

[2] K. Bhattacharya and G. Ravichandran, "Ferroelectric perovskites for electromechanical actuation," *Acta Materialia*, 51, pp. 5941–5960, 2003.

[3] T.R. Braun and R.C. Smith, "FPGA-based model implementation for real-time control of smart material systems operating in hysteretic regimes," Cansmart 2007, International Workshop on Smart Materials and Structures, Montreal, Quebec, CN, October 10-11, 2007.

[4] T.R. Braun and R.C. Smith, "High speed model implementation and inversion techniques for ferroelectric and ferromagnetic transducers," *Journal of Intelligent Material Systems and Structures*, 19(11), pp. 1295–1310, 2008.

[5] E. Burcsu, G. Ravichandran and K. Bhattacharya, "Large electrostrictive actuation of barium titanate single crystals," *Journal of the Mechanics and Physics of Solids*, 52, pp. 823–846, 2004.

[6] J.M. Ernstberger, *High Speed Parameter Estimation for a Homogenized Energy Model,* PhD Dissertation, North Carolina State University, Raleigh, NC, 2008.

[7] Z. Hu, R.C. Smith and J.M. Ernstberger, "Data driven techniques to estimate parameters in a rate-dependent ferromagnetic hysteresis model," *Physica B*, to appear.

[8] Z. Hu, R.C. Smith, M. Hays and W.S. Oates, "Statistical parameter estimation and uncertainty quantification for macro-fiber composites operating in nonlinear and hysteretic regimes," proceedings of the 50th IEEE Conference on Decision and Control and European Control Conference, Orlando, FL, December 12-15, pp. 2764–2769. 2011.

[9] J.E. Huber, "Micromechanical modelling of ferroelectrics," *Current Opinion in Solid State and Materials Science*, 9, pp. 100-106, 2005.

[10] B. Jaffe, W.R. Cook, Jr., and H. Jaffe, *Piezoelectric Ceramics*, Academic Press, New York, 1971.

[11] N.L. Johnson and S. Kotz, *Continuous Univariate Distributions — I Distributions in Statistics*, John Wiley and Sons, New York, 1970.

[12] S.-J. Kim and S. Seelecke, "A rate-dependent three-dimensional free energy model for ferroelectric single crystals," *International Journal of Solids and Structures*, 44, pp. 1196–1209, 2007.

[13] C.M. Landis, "Non-linear constitutive modeling of ferroelectrics," *Current Opinion in Solid State and Materials Science,* 8, pp. 59–69, 2004.

[14] C.S. Lynch, "The effect of uniaxial stress on the electro-mechanical response of 8/65/35 PLZT, *Acta Materialia*, 44(10), pp. 4137–4148, 1996.

[15] J. McMahon, J. Crews and R.C. Smith, "Approximate inversion techniques for the ferroelectric homogenized energy model for ferroelectric materials," preprint.

[16] C. Miehe and D. Rosato, "A rate-dependent incremental variational formulation of ferroelectricity," *International Journal of Engineering Science*, 49, pp. 466–496, 2011

[17] C. Sherman and J.L. Butler, *Transducers and Arrays for Underwater Sound*, Springer Science and Business Media, New York, 2007.

[18] R.C. Smith, *Smart Material Systems: Model Development*, SIAM, Philadelphia, PA, 2005.

[19] R.C. Smith and Z. Hu, "The homogenized energy model (HEM) for characterizing polarization and strains in hysteretic ferroelectric materials: Material properties and uniaxial model development," *Journal of Intelligent Material Systems and Structures*, submitted.

[20] R.C. Smith, A.G. Hatch, B. Mukherjee and S. Liu, "A homogenized energy model for hysteresis in ferroelectric materials: General density formulation," *Journal of Intelligent Material Systems and Structures*, 16(9), pp. 713-732, 2005.

[21] R.C. Smith, S. Seelecke, Z. Ounaies and J. Smith, "A free energy model for hysteresis in ferroelectric materials," *Journal of Intelligent Material Systems and Structures*, 14(11), pp. 719–739, 2003.

[22] J.C. Spall, *Introduction to Stochastic Search and Optimization*, John Wiley and Sons, Hoboken, NJ, 2003.

[23] N. Uchida and T. Iketa, "Temperature and bias characteristics of $Pb(Zr,Ti)O_3$ families ceramics," *Japanese Journal of Applied Physics*, 4(11), pp. 867–880, 1965.

[24] A. York, *Experimental characterization and modeling of electro-mechanically coupled ferroelectric actuators,* PhD Dissertation, North Carolina State University, Raleigh, NC, 2008.

[25] A. York and S. Seelecke, "Experimental study of the electro-mechanical switching behavior of a piezoelectric stack actuator," Proceedings of the SPIE, 6929:692907, 2008.

[26] D. Zhou, M. Kamlah and D. Munz, "Rate dependence of soft PZT ceramics under electric field loading," Proceedings of the SPIE, 4333, pp. 64–70, 2001.